Free Long-Wave Transformation in the Nearshore Zone through Partial Reflections

STEPHANIE CONTARDO,[a,b] RYAN J LOWE,[c] FRANCOIS DUFOIS,[d,e] JEFF E HANSEN,[b] MARK BUCKLEY,[f] AND GRAHAM SYMONDS[b]

[a] *CSIRO Environment, Crawley, Western Australia, Australia*
[b] *School of Earth Sciences, The University of Western Australia, Crawley, Western Australia, Australia*
[c] *Oceans Graduate School, The University of Western Australia, Crawley, Western Australia, Australia*
[d] *Pacific Community Center for Ocean Science, Pacific Community (SPC), Nouméa, New Caledonia*
[e] *IFREMER, DYNECO/DHYSED, Plouzané, France*
[f] *St. Petersburg Coastal and Marine Science Center, U.S. Geological Survey, St. Petersburg, Florida*

(Manuscript received 17 May 2022, in final form 27 October 2022)

ABSTRACT: Long waves play an important role in coastal inundation and shoreline and dune erosion, requiring a detailed understanding of their evolution in nearshore regions and interaction with shorelines. While their generation and dissipation mechanisms are relatively well understood, there are fewer studies describing how reflection processes govern their propagation in the nearshore. We propose a new approach, accounting for partial reflections, which leads to an analytical solution to the free wave linear shallow-water equations at the wave-group scale over general varying bathymetry. The approach, supported by numerical modeling, agrees with the classic Bessel standing solution for a plane sloping beach but extends the solution to arbitrary alongshore uniform bathymetry profiles and decomposes it into incoming and outgoing wave components, which are a combination of successively partially reflected waves lagging each other. The phase lags introduced by partial reflections modify the wave amplitude and explain why Green's law, which describes the wave growth of free waves with decreasing depth, breaks down in very shallow water. This reveals that the wave amplitude at the shoreline is highly dependent on partial reflections. Consistent with laboratory and field observations, our analytical model predicts a reflection coefficient that increases and is highly correlated with the normalized bed slope (bed slope relative to wave frequency). Our approach shows that partial reflections occurring due to depth variations in the nearshore are responsible for the relationship between the normalized bed slope and the amplitude of long waves in the nearshore, with direct implications for determining long-wave amplitudes at the shoreline and wave runup.

KEYWORDS: Ocean; Dynamics; Gravity waves; Shallow-water equations; Wind waves

1. Introduction

Long waves with frequencies between 0.005 and 0.05 Hz, also referred to as infragravity waves, are low-frequency gravity waves that fall within the frequency range forced by wind-wave groups. Free long waves (FLW) generated by wave group forcing were first identified by Munk (1949) and Tucker (1950). These infragravity waves are especially important in the nearshore ocean, where they can make a dominant contribution to water motion in the surf zone (Elgar et al. 1992; Guedes et al. 2013; Reniers et al. 2002; Ruessink 1998; Thornton and Guza 1982) and play an important role in coastal inundation (Cheriton et al. 2016; Merrifield et al. 2014; Péquignet et al. 2009; Roelvink et al. 2009) and beach erosion (Russell 1993; van Rooijen et al. 2012). Therefore, the accurate prediction of the dynamics of long waves in surf zones, including their generation, propagation, and dissipation, is crucial to assess wave-driven coastal hazard risk.

The generation of FLWs results from radiation stress forcing from wind-wave groups approaching the surf zone (Longuet-Higgins and Stewart 1962). Generation can be triggered by three main mechanisms: breakpoint forcing (Symonds et al. 1982), bound wave release (Masselink 1995; Longuet-Higgins and Stewart 1962), and by depth variations (Contardo et al. 2021; Mei and Benmoussa 1984; Nielsen 2017; Moura and Baldock 2019; Liao et al. 2021). These mechanisms have been identified in numerical modeling, laboratory experiments, and field observations (Masselink 1995; Contardo and Symonds 2013; Pomeroy et al. 2012; Inch et al. 2015; Moura and Baldock 2017).

The detailed processes that govern how FLWs propagate through the surf zone (i.e., after their generation) have generally been less well studied. A basic description of the propagation of FLWs is usually assumed where the FLWs are approximated to be sinusoidal and shoal in response to conservation of wave energy flux, where the amplitude theoretically follows Green's law (Green 1838) as $h^{-\alpha}$, where h is local depth and α is the growth rate (theoretically equal to 0.25). However, in this theory, partial reflections, defined here as local reflections occurring over depth variations, are neglected (Koh and Le Méhauté 1966; Svendsen and Hansen 1977), which, according to Koh and Le Méhauté (1966), is only valid for mild bed slopes (<0.025). In many cases, partial reflections are not negligible. Such situations would include the forereef of a fringing reef where the slope is steep (Pomeroy et al. 2012; Péquignet et al. 2014; van Dongeren et al. 2013; Buckley et al. 2018), the sandbar on a barred beach (Contardo and Symonds 2013), and near the shoreline where they can generate partial standing patterns (Baldock 2006; Lara et al. 2010).

Corresponding author: Stephanie Contardo, stephanie.contardo@csiro.au

DOI: 10.1175/JPO-D-22-0109.1

Reflection processes become increasingly important in shallower water, with local reflection coefficients increasing with decreasing depth, and therefore can be very important in the swash zone where waves interact with the shoreline. Wave runup, defined as the maximum vertical elevation of water level at the shoreline, tends to be correlated with long-wave amplitude (Watson et al. 1994; Ruju et al. 2014; Baldock 2006). The approaches used to predict runup are either empirical (Stockdon et al. 2006) or numerical (Fiedler et al. 2020, 2018; Quataert et al. 2020; de Beer et al. 2021), with the exception of Madsen and Fuhrman (2008), who provide analytical solutions for long waves and tsunamis. In two (horizontal) dimensions, edge waves may also develop as seaward propagating FLWs propagate back toward the shore, after being refracted and reflected, forming interference patterns (Contardo et al. 2019; Bowen and Guza 1978; Eckart 1951; Guza and Davis 1974; Chao and Pierson 1972; Almar et al. 2018).

Strong reflections of FLWs from steeply sloping bathymetry profiles can also play a dominant role in establishing low-frequency standing waves that become dominant sources of wave runup. For example, in fringing reef environments with steep fore reef slopes, resonant amplification of long waves can occur when low-frequency forcing by wave groups matches the natural frequencies for standing waves propagating across reef flat (Péquignet et al. 2009; Torres-Freyermuth et al. 2012; Cheriton et al. 2016; Gawehn et al. 2016; Buckley et al. 2018). The amplification of these long waves thus results from the strength of partial reflections of outgoing long waves at the crest of the steep forereef that return long waves back to the shoreline.

The total reflection coefficient, defined either as the ratio of outgoing to incoming wave amplitudes or energy fluxes, is also influenced by a range of long-wave dissipation processes (Battjes 1974), including bottom friction (Henderson and Bowen 2002), nonlinear transfers of energy back to sea-swell frequencies (Henderson et al. 2006; Thomson et al. 2006; Guedes et al. 2013; Ruju et al. 2012), and depth-limited breaking (Battjes et al. 2004; van Dongeren et al. 2007; Ruju et al. 2012). Therefore, the measured reflection coefficient has been used as a proxy for the level of long-wave dissipation in field observations (Sheremet et al. 2002; de Bakker et al. 2014; Elgar et al. 1994, 1992; Okihiro and Guza 1995; Bertin et al. 2020), laboratory experiments (Padilla and Alsina 2017; Battjes et al. 2004), and in numerical model applications (van Dongeren et al. 2007).

Reflection coefficients are known to increase with bed slope and decrease with wave frequency, with both effects generally incorporated into empirical parameterizations of reflection, namely, a surf similarity parameter (Iribarren number) (Battjes 1974; Iribarren Cavanilles and Casto Nogales 1949) or the normalized bed slope parameter (Battjes et al. 2004). Various field and laboratory experiments have confirmed that the reflection coefficient increases with normalized bed slope (van Dongeren et al. 2007; Guedes et al. 2013; de Bakker et al. 2014; Padilla and Alsina 2017; Okihiro and Guza 1995; Bertin et al. 2020).

In analytical studies of long-wave transformation, the total wave amplitude, rather than its decomposition into incoming and outgoing components, is usually predicted. The linear shallow-water equation on a sloping bottom is a Bessel differential equation of zeroth order and its analytical solutions are in the form of Bessel functions (Dean 1964; Symonds et al. 1982; Eckart 1951; Abdelrahman 1986; Friedrichs 1948; Suhayda 1974; Symonds and Bowen 1984; Synolakis 1991). Since the solutions conserve energy, they account for all reflections, i.e., both full (at the shoreline) and partial.

The question of a formulation for reflection of free waves has been addressed mostly for short waves (wind-sea and swell) and inferred empirically based on wave breaking dissipation (Battjes 1974; Ursell et al. 1960; Miche 1951), which motivated the development of empirical predictive formulations that are widely used in coastal engineering applications (Miche 1951; Seelig and Ahrens 1981; Madsen and White 1976; Zanuttigh and van der Meer 2008; Zhang et al. 2021; Dean 1964). Analytical studies of reflection over bathymetry profiles exist, but for specific cases only; for example, Didenkulova et al. (2009) for specific convex bathymetry profiles; Bayındır and Farazande (2021) for power-law profiles; and Mei (1989), who proposed a solution for slowly varying depth, based on the classical WKB approximation, where a reflection coefficient is calculated for a section of slope.

In the present study, we propose analytical expressions for the incoming and outgoing components of a FLW propagating in the cross-shore direction in shallow water over a variable depth profile in the absence of dissipation. We account for upslope and downslope partial reflections and assess the effect of normalized bed slope on the propagation. We first describe the method leading to our analytical model based on partial reflections, then we apply our partial reflection approach to various common nearshore bathymetry profiles (sloping beach, barred beach, fringing reef) and show how these results can help explain some previous observations of long-wave dynamics over these profiles. We finally extend the results to cases where long waves are assumed to dissipate at an inshore location (e.g., due to breaking). The study reveals that continuous partial reflections occurring due to depth variations in the nearshore are responsible for the strong dependency between the normalized bed slope and the amplitude of long waves in the nearshore.

2. Partial reflection analytical model

The approach we develop here is built upon existing theory of wave reflection over a single step (summarized in appendix A). By discretizing an arbitrary cross-shore bathymetry profile into a series of steps, through superposition we investigate the role of partial reflections over common nearshore morphologies. To develop this approach, we initially consider the case where there is no long-wave dissipation. The case where dissipation is included will be discussed in section 4e.

Following the approach adopted by Contardo et al. (2021) to describe the generation of FLWs over varying bathymetry, the bathymetry is discretized into a succession of small steps, of width dx, such that the equations governing reflection and transmission over a single step are repeated for each depth variation, as presented schematically in Fig. 1. Therefore, the total incoming waves (propagating shoreward) at a given location are a combination of waves reflected an even number (including zero) of times. Similarly, outgoing waves (propagating seaward) are a combination of waves reflected an odd number

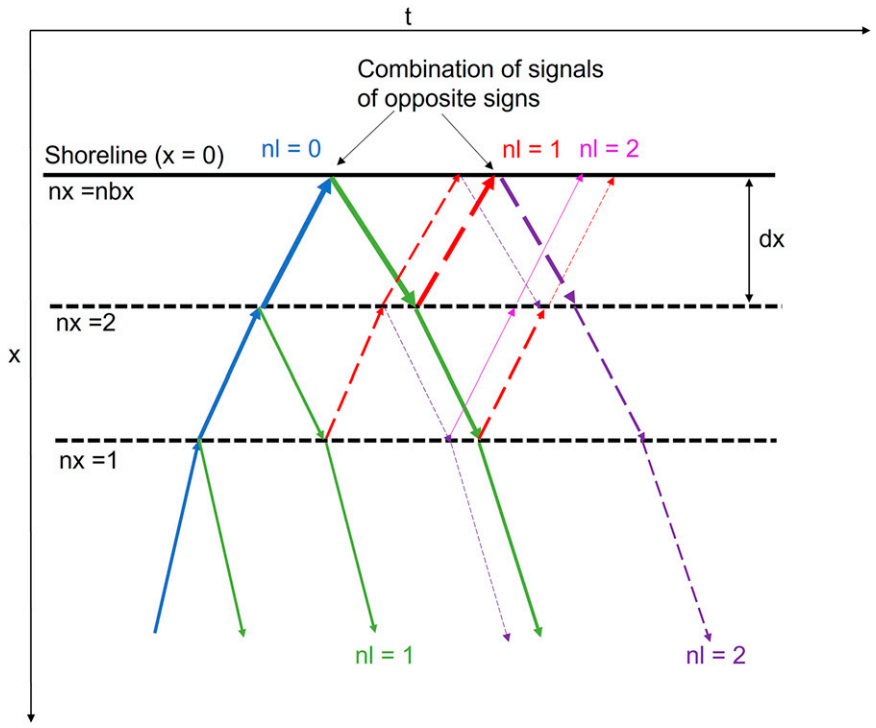

FIG. 1. Schematic of the series of reflected waves (illustrating four reflections), over three steps. Blue: level 0 (no reflection), green: level 1 outgoing, red: level 1 incoming, purple: level 2 outgoing, and magenta: level 2 incoming. The dashed lines denote a reflected signal with opposite phase. The line thickness gives a qualitative indication of the wave amplitude.

of times. As the number of reflections increases, the amplitude within the series of reflected waves decreases and becomes negligible.

We start by calculating the amplitude A_{in} of the initial incoming wave, i.e., the wave transmitted without any reflections (blue arrows in Fig. 1), at a given cross-shore location $x(\text{nx})$:

$$A_{\text{in}}(\text{nx}) = A_0 \prod_{j=1}^{\text{nx}-1} k_t(j), \tag{1}$$

where A_0 is the amplitude of the incident wave at the bottom of the slope, $k_t(\text{nx})$ is the transmission coefficient between the steps nx and nx + 1, $k_t(0) = 1$ (on the first step), and Π is the product notation. We introduce the complex amplitude: $\hat{A}(x) = Ae^{i(\kappa x+\varphi)}$. By including the phase lag arising from the propagation over the steps, the complex incoming amplitude is

$$\hat{A}_{\text{in}}(\text{nx}) = A_0 \prod_{j=0}^{nx-1} k_t(j) \exp\left[i \sum_{j=1}^{nx} \varphi_{dx}(j)\right]. \tag{2}$$

where $\varphi_{dx}(\text{nx})$ is the phase difference corresponding to the propagation time over the finite step nx:

$$\varphi_{dx}(\text{nx}) = \frac{dx}{c}\omega. \tag{3}$$

In this first estimation of the amplitude of the incoming wave, the number of reflections is zero. We refer to this as level 0 (nl = 0). The next step is to account for partial reflections by superimposing the signals from reflected waves.

We calculate the amplitude A_{out} of the outgoing wave by assuming total reflection at the shoreline (and neglecting all other reflections):

$$\hat{A}_{\text{out}}(\text{nx}) = \hat{A}_{\text{in}}(\text{nx}) \exp\left[2i \sum_{j=\text{nx}}^{\text{nbx}} \varphi_{dx}(j)\right], \tag{4}$$

with nbx the total number of steps. Since the reflection at the shoreline is by definition the total reflection, due to the transmitted wave being zero, in the absence of dissipation the outgoing and incoming waves have equal amplitudes at all cross-shore locations, and their phase difference is determined by the propagation time from their cross-shore position to the shoreline and back.

In this initial example, the waves have been assumed to only reflect at the shoreline. However, in reality the incident wave reflects successively at each step, the reflected waves deshoal as they move into deeper water, and the reflected signals combine with a time lag (Fig. 1). We now consider the influence of these successive partial reflections.

We define nl as the number of additional downslope reflections that is accounted for in the combined wave field. As nl increases, another level of reflection is added. For instance, the outgoing signal at nl = 1 (green arrows in Fig. 1) is the

combination of waves reflected on steps nx = 1, nx = 2 and at the shoreline (nx = nbx). Therefore, we calculate the amplitudes iteratively and the amplitude of the total outgoing wave is, for nl ≥ 1:

$$\begin{aligned}\hat{A}_{\mathrm{out,nl}}(\mathrm{nx}) &= \hat{A}_{\mathrm{in,nl-1}}(\mathrm{nx})k_r(\mathrm{nx})\exp[i\varphi_{dx}(\mathrm{nx})]\\ &\quad+\hat{A}_{\mathrm{in,nl-1}}(\mathrm{nx}+1)k_r(\mathrm{nx}+1)k_t^{\mathrm{inv}}(\mathrm{nx})\\ &\quad\times\exp\{i[\varphi_{dx}(\mathrm{nx}+1)+\varphi_{dx}(\mathrm{nx})]\}\\ &\quad+\hat{A}_{\mathrm{in,nl-1}}(\mathrm{nx}+2)k_r(\mathrm{nx}+2)k_t^{\mathrm{inv}}(\mathrm{nx}+1)k_t^{\mathrm{inv}}(\mathrm{nx})\\ &\quad\times\exp\{i[\varphi_{dx}(\mathrm{nx}+2)+\varphi_{dx}(\mathrm{nx}+1)+\varphi_{dx}(nx)]\}\\ &\quad+\cdots\\ &=\sum_{j=\mathrm{nx}}^{\mathrm{nbx}}\hat{A}_{\mathrm{in,nl-1}}(j)k_r(j)\prod_{l=\mathrm{nx}}^{j-1}k_l^{\mathrm{inv}}(l)\exp\left[i\sum_{l=\mathrm{nx}}^{j}\varphi_{dx}(l)\right],\end{aligned}\tag{5}$$

with $k_t^{\mathrm{inv}}(\mathrm{nx})$ the downslope transmission coefficient between $h(\mathrm{nx}+1)$ and $h(\mathrm{nx})$ defined according to Eq. (A7):

$$k_t^{\mathrm{inv}}=\frac{2\kappa_{\mathrm{sea}}}{\kappa_{\mathrm{shore}}+\kappa_{\mathrm{sea}}}=k_t\frac{\kappa_{\mathrm{sea}}}{\kappa_{\mathrm{shore}}}.\tag{6}$$

The next reflection to occur is a downslope reflection, which is followed by a succession of reflections occurring alternately upslope and downslope. Therefore, for nl ≥ 1, the incoming complex amplitude is

$$\begin{aligned}\hat{A}_{\mathrm{in,nl}}(\mathrm{nx}) &= \hat{A}_{\mathrm{out,nl}}(\mathrm{nx})k_r(\mathrm{nx}-1)\exp[i\varphi_{dx}(\mathrm{nx})]\\ &\quad+\hat{A}_{\mathrm{out,nl}}(\mathrm{nx}-1)k_r(\mathrm{nx}-2)k_t(\mathrm{nx}-1)\\ &\quad\times\exp\{i[\varphi_{dx}(\mathrm{nx}-1)+\varphi_{dx}(\mathrm{nx})]\}\\ &\quad+\hat{A}_{\mathrm{out,nl}}(\mathrm{nx}-2)k_r(\mathrm{nx}-3)k_t(\mathrm{nx}-2)k_t(\mathrm{nx}-1)\\ &\quad\times\exp\{i[\varphi_{dx}(\mathrm{nx}-2)+\varphi_{dx}(\mathrm{nx}-1)+\varphi_{dx}(\mathrm{nx})]\}\\ &\quad+\cdots\\ &=\sum_{j=1}^{\mathrm{nx}}\hat{A}_{\mathrm{out,nl}}(j)k_r(j-1)\prod_{l=j}^{\mathrm{nx}-1}k_t(l)\exp\left[i\sum_{l=j}^{\mathrm{nx}}\varphi(l)\right].\end{aligned}\tag{7}$$

At a cross-shore location $x = \mathrm{nx}\times dx$, the total reflection coefficient R, which accounts for all the local reflections, can thus be defined here as the ratio of cumulative outgoing to incoming wave amplitudes:

$$R(x)=\frac{A_o(x)}{A_i(x)},\tag{8}$$

or where alternatively R^2 represents the reflection coefficient based on energy flux.

Based on this model, the amplitude of the outgoing wave is dependent on the bed slope, the depth at the model offshore boundary and the wave frequency, due to the phase lags generated over each step [Eq. (3)] being dependent on the wave frequency. Using this model, we calculate the amplitude of the incoming and outgoing FLWs for a frequency $f = 0.005$ Hz and for three slope values: $\beta = 0.05$, 0.005, and 0.001. The amplitude of the incident wave, A_0, is defined at the reference cross-shore position X, which could, for example, represent the offshore extent of the surf zone, where FLWs originate. For these calculations, a flat bottom is assumed beyond X, so no reflections occur further offshore. In this example, $X = 2000$ m. This value is chosen so that at least a whole wavelength can be observed (about 1800, 180, and 37 m for $\beta = 0.05$, 0.005, and 0.001, respectively). As we account for an increasing number of reflections, the total reflection coefficient tends toward 1 to ensure conservation of energy (Fig. 2). Convergence is achieved rapidly for a very mild slope ($\beta = 0.001$), for instance, after three iterations, but it takes over 20 iterations for $\beta = 0.05$ to converge. Hereafter, we will apply the analytical model with nl = 50 to ensure convergence is reached, for all slopes considered in this study (not shown), and unless specified otherwise, the amplitudes of the incoming and outgoing FLWs will be calculated as $A_{i\mathrm{FLW}} = A_{\mathrm{in}}(\mathrm{nl}=50)$ and $A_{o\mathrm{FLW}} = A_{\mathrm{out}}(\mathrm{nl}=50)$, respectively. Note that in applications of the model that follow, amplitudes A will be nondimensionalized with the amplitude of the incident FLW at X (denoted A^*, where the * will be used to denote nondimensional variables) and $x^* = x/X$ is the nondimensional cross-shore distance parameter.

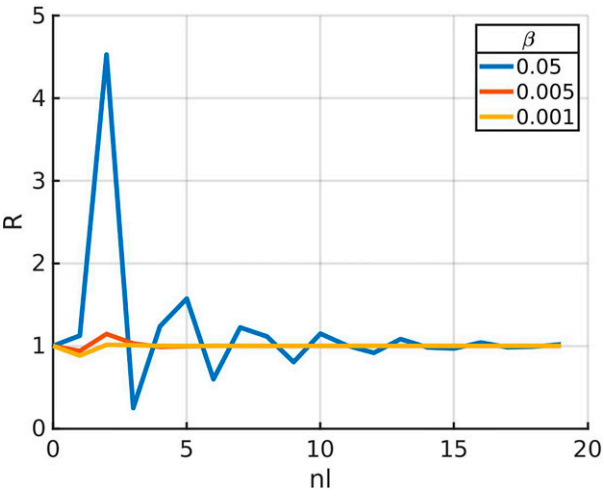

FIG. 2. Calculated total reflection coefficient vs number of iterations (nl) for three bed slopes.

3. Comparison with Bessel analytical standing wave solutions for a plane sloping bottom

Analytical solutions based on linear wave theory are available for predicting long-wave propagation over a mild sloping bottom. The shallow-water equation for slowly varying depth (i.e., Dean 1964) is

$$\frac{\partial}{\partial x}\left(gh\frac{\partial\zeta}{\partial x}\right)+\frac{\partial^2\zeta}{\partial t^2}=0.\tag{9}$$

Given a linear slope β and assuming a harmonic wave, Eq. (9) becomes

$$x\frac{\partial^2\zeta}{\partial x^2}+\frac{\partial\zeta}{\partial x}-\frac{\omega^2}{g\beta}\zeta=0,\tag{10}$$

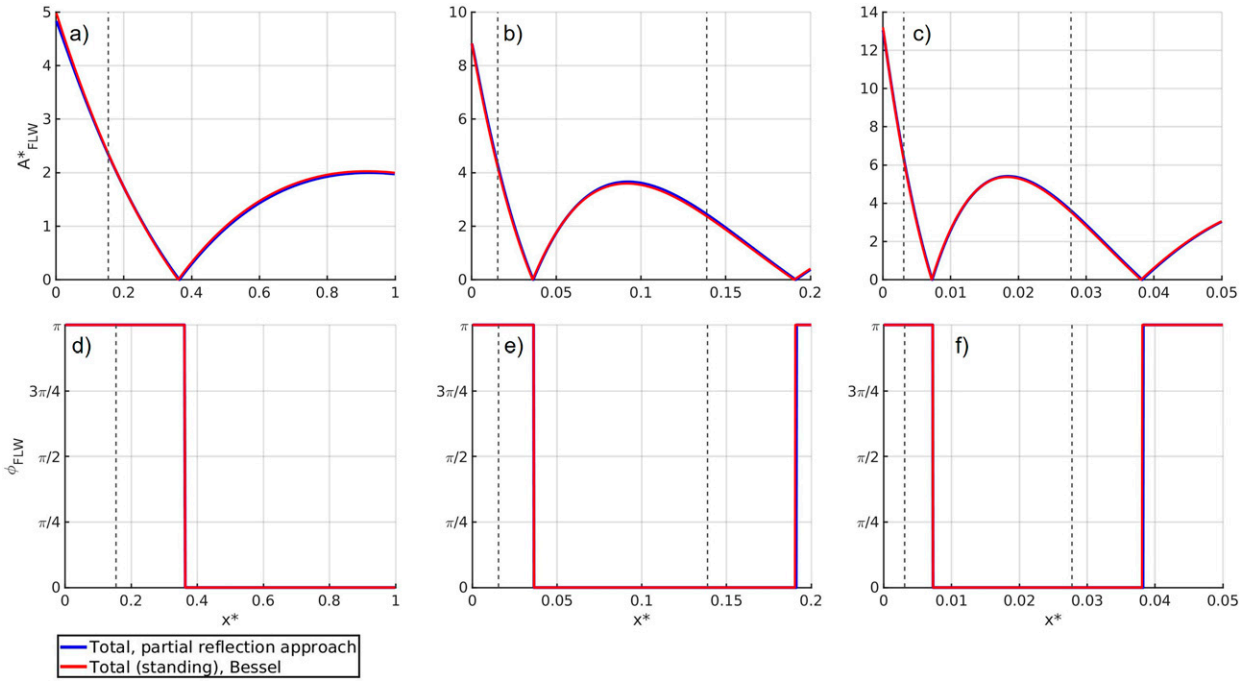

FIG. 3. Theoretical FLW nondimensional (a)–(c) total amplitudes A^*_{FLW} and (d)–(f) phase lags ϕ_{FLW} for plane sloping bottom, comparing predictions from our partial reflection approach with Bessel function solutions, for $f = 0.005$ Hz and three values of slope β: 0.05, 0.005, and 0.001. The shoreline is at $x^* = 0$. Vertical dashed gray lines denote the theoretical locations where the nodes would be located in the absence of partial reflections.

which is a Bessel equation. For a propagating wave, the Bessel solutions are in the form (Symonds et al. 1982; Eckart 1951; Dean 1964):

$$J_0\left(2\sqrt{\frac{\omega^2 x}{g\beta}}\right)\cos(\omega t) - Y_0\left(2\sqrt{\frac{\omega^2 x}{g\beta}}\right)\sin(\omega t), \tag{11}$$

with J_0 a Bessel function of the first kind and Y_0 a Bessel function of the second kind, both of order zero. If the shoreline is at the shoreward boundary of the sloping section, the solution in Y_0 is excluded as it tends to infinity for $x = 0$, and the solution is a standing wave:

$$J_0\left(2\sqrt{\frac{\omega^2 x}{g\beta}}\right)\cos(\omega t). \tag{12}$$

While the approach we developed (section 2) is valid for any arbitrary bathymetry profile, here we calculate solutions for the plane sloping bottom case using our approach (section 2) and compare these results to the analytical Bessel solutions. We calculate the amplitudes and phase lags, at $f = 0.005$ Hz, for three values of slope β: 0.05, 0.005, and 0.001.

The amplitudes of the outgoing and incoming waves are equal (not shown), both with our approach where we assume total reflection (i.e., no dissipation) at the shoreline and using Bessel solutions, as the total solution is a standing wave. While we use local reflection and transmission coefficients (k_r and k_t, respectively) to calculate the complex amplitudes of the incoming and outgoing waves, the system conserves energy and therefore the total reflection coefficient (R), defined by Eq. (8), equals 1.

Figure 3 shows a comparison of the amplitudes and phase lags of the standing wave calculated using our approach (blue solid lines, including partial reflections) developed in section 3 with the Bessel standing wave solutions (red solid lines), as a function of the nondimensional cross-shore distance x^*. In all cases, the cross-shore profile of the total (standing wave) amplitudes and phase lags are in good agreement.

In Fig. 3 a standing pattern is well defined (i.e., the amplitude is zero at the location of the nodes) despite the phase lags present, because of the total reflection at the shoreline and conservation of energy. The phase lags introduced by partial reflections modify the amplitude of the standing waves and shift the location of the nodes. With no partial reflection, the nodes would be located at the cross-shore positions x_{node} (indicated in vertical dashed lines in Fig. 3) according to (i.e., Buckley et al. 2018; Symonds and Bowen 1984)

$$f_{\mathrm{node}} = \frac{1}{4}(2n-1)\left(\int_{x_{\mathrm{node}}}^{x_0}\frac{1}{\sqrt{gh}}dx\right)^{-1} \tag{13}$$

with n the node number. In the case of a plane beach, we obtain

$$x_{\mathrm{node}} = g\beta\left(\frac{2n-1}{8f_{\mathrm{node}}}\right)^2. \tag{14}$$

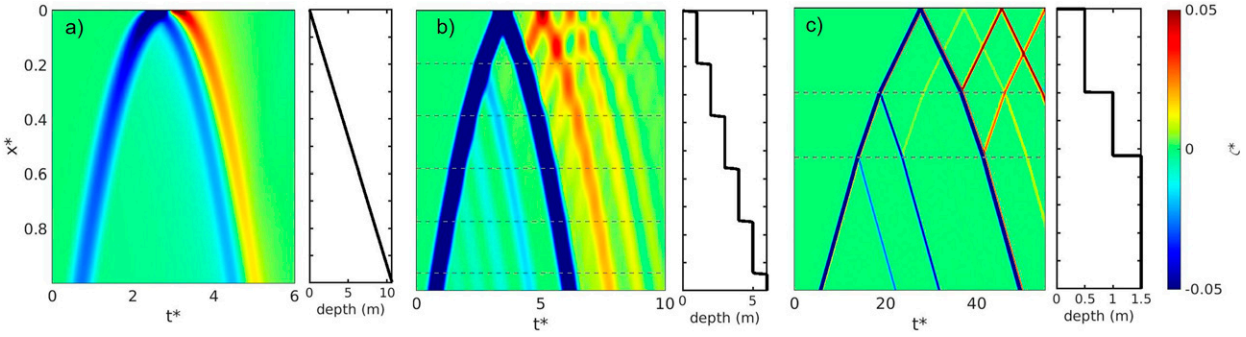

FIG. 4. Nondimensional total FLW elevation as a function of nondimensional time (horizontal axis) and cross-shore position (vertical axis), for (a) a plane slope with $\beta = 0.005$, (b) a succession of small steps (0.2 m every 200 m), and (c) a two-step configuration, forced by a single transient wave. Cross-shore bathymetry profiles are represented on the right side of each color plot. The dashed horizontal lines in (b) represent the location of the step depth changes.

The actual node frequencies, accounting for partial reflections, are therefore underestimated by Eq. (13), but in agreement with the Bessel solutions.

4. Results and discussion

With the analytical model based on partial reflections verified in appendix B, we apply it here to demonstrate that the partial reflection approach can be used to help interpret and provide new insight into previously observed features of long-wave propagation in the nearshore. We first focus on partial reflection processes at the shoreline then apply the analytical model to a plane sloping beach, a realistic barred beach, and an idealized fringing reef, and study the role of partial reflections, first assuming complete reflection at the shoreline, then investigating the total reflection coefficient for the case where the bathymetry near the shoreline is truncated, as a proxy for dissipation of the FLW occurring at some shallow inshore depth.

a. *Shoreline processes*

In appendix B, the amplitude of the FLWs decreased at the shoreline as β increased (i.e., Fig. B1 for the plane beach) and as f decreased (i.e., Fig. B3 for the barred beach profile), which we now show here is due to the presence of phase lags resulting from the occurrence of continuous partial reflections. To visualize how the processes of reflection affect the phase lag and support this interpretation, we consider the numerical model results for a plane sloping beach ($\beta = 0.004$, $f = 0.01$ Hz) as in appendix B, section a, and compare these results to a case with two large steps, as the latter will be useful to explain the former. The widths of the steps are chosen large enough so the waves can be clearly isolated ($h = 0.5$ m for $x < 3700$ m, $h = 1$ m for $3700 \leq x < 5200$ m and $h = 1.5$ m for $x \geq 5200$ m). The model is forced with a negative single (transient) wave, as opposed to periodic waves, to enable the incident and radiated long waves to be clearly separated in time and space and their propagation paths to be visualized (Baldock 2006; Contardo et al. 2021; Watson et al. 1994).

For the plane sloping beach case, the reflection of the negative incoming signal is a combination of a negative signal and a positive signal (Fig. 4a). We use the two-step configuration (Fig. 4c) to visualize the reflection processes that occur continuously for the slope case and explain why the reflected signal has both positive and negative components. The interpretation is as follows. Once the level 0 incoming (negative) signal has reflected at the shoreline, it reflects again at the next depth change as it propagates seaward. While reflecting shoreward, the signal changes sign (the reflected wave is in antiphase with the incident wave). It reflects in the same way, on each depth change, so that the signal at the shoreline is a combination of the level 0 incoming wave (defined earlier as the blue arrow in Fig. 1), of the level 1 incoming waves reflected twice (red dashed arrows in Fig. 1) and of higher level incoming waves. In the linear slope case, waves reflecting near the shoreline are only slightly smaller than the level 0 signal, they overlap with it, and their phase lag with the level 0 wave is small; whereas waves reflecting further from the shoreline are smaller and their phase lag with the level 0 signal is larger. Figure 4b shows the elevation for an intermediary bathymetry profile, with finer steps than in Fig. 4c. Partial standing wave patterns appear as the reflected components of the signal overlap.

The interactions between the incoming and reflected waves is further illustrated with a synthetic example where we consider two sinusoidal waves (Fig. 5). The first wave represents a level 0 incoming wave (Fig. 5, dashed lines) and the second wave represents a level 1 wave (Fig. 5, dash–dot lines), reflected twice (thus also incoming). The amplitudes of the waves are the same in both cases but in one case the non dimensional time lag dt^* between the two waves is >0.5 (Fig. 5a) and in the other case it is <0.5 (Fig. 5b). When $dt^* > 0.5$, the total wave that results from the combination of the level 0 and level 1 waves is larger than the level 0 wave, and when the lag is $dt^* < 0.5$ the total wave is smaller than the level 0 wave. In addition, a time lag is introduced by the presence of the level 1 wave (the total signal precedes the level 0 signal). Therefore, the addition of the level 1 wave to the level 0 wave introduces a time lag and either increases or decreases the total amplitude

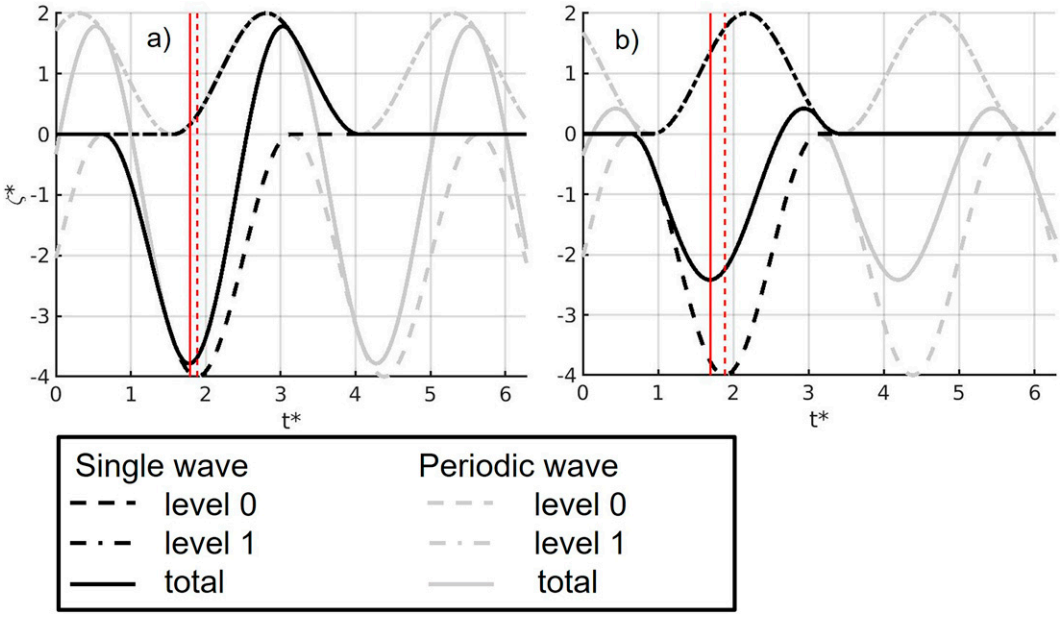

FIG. 5. Synthetic example of combinations of positive and negative sinusoidal wave signals at the shoreline in both single and periodic form for (a) $dt^* > 0.5$ and (b) $dt^* < 0.5$. In this example, the nondimensional amplitude of the negative signal (level 0) is 2 and the amplitude of the positive signal (level 1) is 1, $f = 0.4$ Hz, and $h = 5$ m. Black lines represent single (transient) waves while gray lines represent periodic signals. The vertical red lines indicate the trough of the incoming wave (dashed line) and total wave (solid line).

depending on the lag between the level 0 wave and the level 1 wave.

The literature provides examples of such observations from experimental and numerical modeling. Figure 5 in Baldock (2006) and Fig. 9 in Lara et al. (2010) represent the sea surface elevation as a function of time and cross-shore position for a plane beach ($\beta = 0.1$) and a beach with two sloping regions ($\beta = 0.05$) separated by a horizontal bottom section, respectively. These figures are similar to Fig. 4a. In Fig. 5 in Baldock (2006), after a positive signal reaches the shoreline, the reflected signal is composed of both a positive and a negative signal, with the outgoing negative signal being (according to our interpretation) the incoming positive signal reflected an odd number (≥ 3) of times. Baldock (2006) mentions an "interference between long waves formed by the different surf zone generation mechanisms" which would reduce the long-wave energy and points out that the negative part of the signal indicates "either reflection higher on the beach or further long wave generation in the swash." In Fig. 9 in Lara et al. (2010), a positive signal also reaches the shoreline, and, with a delay, a negative signal also reaches the shoreline, which according to our interpretation is the incoming positive signal reflected an even number of times. Lara et al. (2010) hypothesize that the signal is being generated within the surf and swash zone. Our models (analytical and numerical) do not include a time-varying shoreline position, yet this signal is observed, suggesting that the shoreline processes observed by Baldock (2006) and Lara et al. (2010) are driven by reflection. Given the apparent role of partial reflections near the shoreline and the direct correlation between runup and shoreline amplitude (Madsen and Fuhrman 2008), runup estimations could benefit from including a partial reflection approach.

b. *Plane sloping beach*

Here we further investigate the processes that govern how partial reflections affect the amplitude and phase of the FLWs as a function of beach slope. The results that follow are presented as a function of the normalized surf zone width χ (Symonds et al. 1982):

$$\chi = \frac{\omega^2 X}{g\beta}. \tag{15}$$

The term X represents the location where the FLWs are generated. This location is generally associated with the short-wave breakpoint where FLWs are generated through both breakpoint forcing (Symonds et al. 1982) and bound wave release (Masselink 1995). However, it can also be the location where FLWs are generated via the depth-variation mechanism (Contardo et al. 2021), offshore of the short-wave breakpoint or inshore of it from remaining short-wave groupiness. In the following, we use the short-wave breaking depth h_b to indicate where the FLWs are generated, although it could simply be replaced by the depth at which FLWs are generated in the case of generation by the depth-variation mechanism.

As X represents the location where the FLWs are generated, we note that for a linear slope it can be replaced with

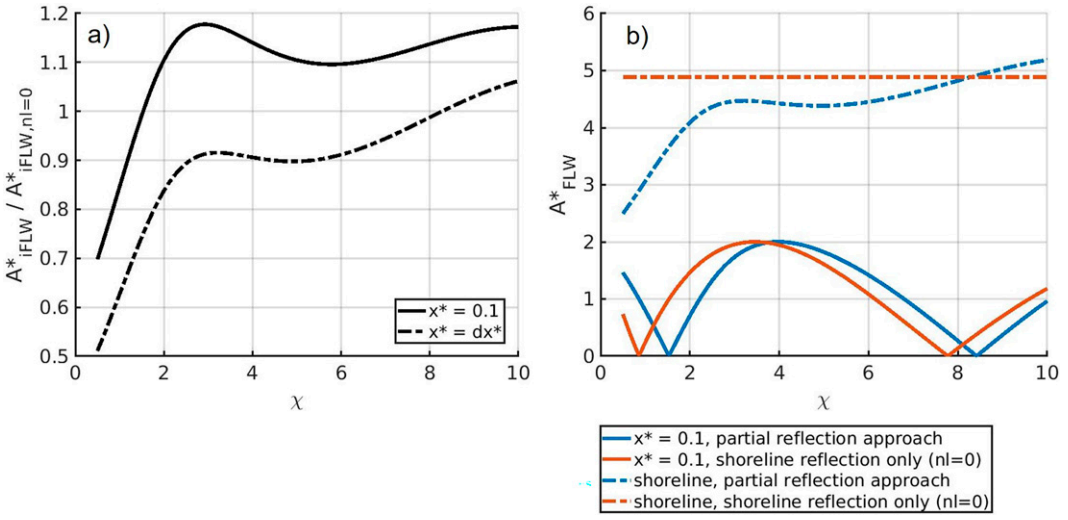

FIG. 6. (a) Ratio of the incoming FLW amplitudes for results based on partial reflection approach ($A^*_{i\mathrm{FLW}}$) divided by results with reflection at the shoreline only ($A^*_{i\mathrm{FLW,nl=0}}$) at two cross-shore locations $x^* = dx^* = 0.01$ (location nearest the shoreline) and $x^* = 0.1$ ($X = 100$ m) and (b) total amplitude for the partial reflection approach and with reflection at the shoreline only (nl = 0) for $f = 0.005$ Hz over a plane sloping beach with β varying between 0.001 and 0.05.

h_b/β, as in Battjes et al. (2004); thus χ can be alternatively expressed as

$$\chi = \frac{\omega^2 h_b}{g\beta^2} = \frac{1}{\beta^2_{\mathrm{norm}}}, \tag{16}$$

with β_{norm} defined as the normalized bed slope:

$$\beta_{\mathrm{norm}} = \frac{\beta}{\omega}\sqrt{\frac{g}{h_b}}. \tag{17}$$

1) INCOMING WAVE

The incoming amplitude and phase calculated at two different locations are normalized with the amplitude and phase calculated without partial reflections (nl = 0), i.e., the case where only shoaling occurs, (Figs. 6a,b), at two locations: $x^* = dx^*$ (the nonzero depth closest to the shoreline) and at $x^* = 0.1$ (a location away from the shoreline). The level 0 case is used as reference as, without partial reflection, the relative amplitude and phase does not vary with χ, as shoaling does not depend on the slope.

The inclusion of partial reflections affects the amplitude and phase of the total incoming wave signal (Fig. 6a). The amplitude, calculated with the partial reflection approach, displays a variable but generally increasing trend, similar to what was observed (but not explained) by Madsen and Fuhrman (2008), whose solutions to the linear shallow water equation for runup (which is analogous to shoreline wave amplitude) on a finite slope attached to a flat bottom present an analogous oscillating response. The amplitude with partial reflections included is higher than the level 0 amplitude for higher χ (1.5 for $x^* = 0.1$ and 8.2 for $x^* = dx^*$), and lower for lower χ.

The trend in Fig. 6a occurs because for small χ (equivalent to a steep normalized bed slope), the signal reflected at the shoreline and then back to the shoreline (nl = 1) does not substantially lag behind the incoming wave (nl = 0). As it is of opposite sign to the incoming signal, the combination results in a total amplitude that is smaller than would be expected from shoaling, as was indicated in Fig. 5b. In contrast, for large χ (equivalent to a mild normalized bed slope), the level 1 and level 0 signals lag each other more substantially so that their combined signal is larger than the amplitude expected from shoaling (Fig. 5a).

Partially transmitted and partially reflected signals combine and form partially standing waves. These partial standing patterns appear as amplitude and phase variations around the general trend. In Fig. 6a, the elevation amplitude at the shoreline is maximum when $\chi = 2.7$, due to the level 1 signal (reflected at the shoreline then reflected back to the shore) being in phase with the level 0 signal; conversely, when $\chi = 5.5$, there is a local minimum because the signal when reflected twice is in antiphase with the incoming signal.

Due to this interference pattern, the wave amplitude growth does not increase as $h^{-\alpha}$, with the growth rate $\alpha = 0.25$ following Green's law. However, we can estimate a mean growth rate over the domain using the present results, as

$$\alpha(x) = -\log_{10}\left[\frac{A_i(x)}{A_i(X)}\right]\Big/\log_{10}\left[\frac{h(x)}{h_b}\right],\ \alpha_m = \langle\alpha(x)\rangle, \tag{18}$$

where the angle brackets represent spatial averaging.

The mean growth rate is represented as a function of β_{norm} for different h_b, which serves as a proxy for the location of long-wave generation (Fig. 7). For $\beta_{\mathrm{norm}} < 0.5$, α_m is between 0.15 and 0.4 and there is no trend in the response to β_{norm}. However, there is a consistent maximum (α_m between 0.4 and 0.5) around $\beta_{\mathrm{norm}} = 0.65$, with α_m then decreasing exponentially past the maximum. Importantly, the growth rate is substantially above Green's law ($\alpha = 0.25$)

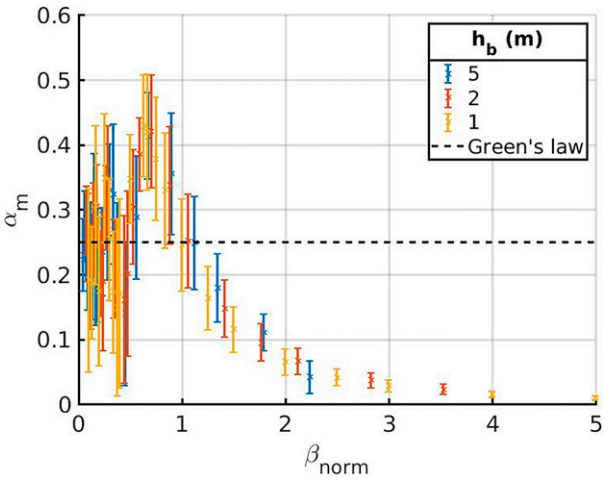

FIG. 7. Mean growth rate α_m of the FLW amplitude [calculated with Eq. (18)] as a function of β_{norm}, for different short-wave breaking depths (FLW generation depths) h_b, calculated for a plane sloping beach with β between 0.01 and 0.05 and f between 0.005 and 0.05 Hz. The horizontal dashed line denotes the value $\alpha = 0.25$ predicted based on Green's law. The error bars represent the standard deviation of $\alpha(x)$.

for $0.7 < \beta_{\text{norm}} < 1$ and lower for $\beta_{\text{norm}} > 1$. We note that a similar trend had been observed close to the shoreline by van Dongeren et al. (2007), although the wave growth reached a lower limit at 0.25. They indicate a transition to conservative shoaling ($\alpha = 0.25$) for $\beta_{\text{norm}} > 1$, which in our results corresponds to $\alpha \leq 0.25$. Values of $\alpha < 0.25$ indicate that the incident (shoreward propagating) transmitted wave is smaller than it would be in the absence of partial reflections. This means that the reflected signal must be taken into account to ensure energy conservation.

2) TOTAL (INCOMING AND OUTGOING)

As there is complete reflection at the shoreline, the outgoing amplitude is equal to the incoming amplitude, and a standing pattern is expected. The total amplitude, at two cross-shore locations, as a function of χ is shown in Fig. 6b. The standing pattern expected is present at $x^* = 0.1$, but it is shifted toward higher χ (i.e., higher frequencies), compared to the approach with reflection at the shoreline only, the nodes being shifted from $\chi = 0.8$ and 7.8 (nl = 0) to 1.5 and 8.4 (partial reflection approach). At $x^* = dx^*$ (shoreline), the level 0 amplitude does not vary with χ, while the amplitude with partial reflections generally increases with some variability (one local maximum and one local minimum) as χ increases. This response is due to interference patterns introduced by the reflections, which are visible as variations around the trend in Fig. 6a.

3) INCOMING AND OUTGOING COMPONENTS IN BESSEL SOLUTIONS

In section 3, we showed that the total (standing) solution based on our partial reflection approach agreed with the standing Bessel solution. Here we extend the comparison to incoming and outgoing components of the solutions.

We decompose the Bessel standing solution into a single incoming wave and a single outgoing wave following Contardo et al. (2018), where the incoming and outgoing solutions for elevation based on the decomposition are, respectively,

$$\zeta_{i\text{FLW,Bessel}} \propto \frac{1}{2}\left[J_0\left(2\sqrt{\frac{\omega^2 x}{g\beta}}\right)\cos(\omega t) - Y_0\left(2\sqrt{\frac{\omega^2 x}{g\beta}}\right)\sin(\omega t)\right] \quad \text{and}$$
$$\zeta_{o\text{FLW,Bessel}} \propto \frac{1}{2}\left[J_0\left(2\sqrt{\frac{\omega^2 x}{g\beta}}\right)\cos(\omega t) + Y_0\left(2\sqrt{\frac{\omega^2 x}{g\beta}}\right)\sin(\omega t)\right]. \tag{19}$$

The amplitudes of the incoming and outgoing waves based on this decomposition are therefore both

$$A_{i/o\text{FLW,Bessel}} \propto \frac{1}{2}\left[J_0\left(2\sqrt{\frac{\omega^2 x}{g\beta}}\right)^2 + Y_0\left(2\sqrt{\frac{\omega^2 x}{g\beta}}\right)^2\right]. \tag{20}$$

Results showing the amplitudes of the incoming wave in Eq. (20), the amplitudes of the incoming solution from the partial reflection approach and the amplitudes following Green's law (shoaling only) are represented in Figs. 8a, 8c, and 8e as a function of the nondimensional cross-shore distance x^*.

First, we compare the partial reflection approach to the Bessel solutions, in terms of amplitudes and phase lags (Fig. 8, blue and red lines). At the shoreline, the incoming wave based on the partial reflection approach is smaller than the Bessel incoming wave and, away from the shoreline, the incoming wave amplitudes are alternately above and below the shoaling curve, because of the interference pattern created by partial reflections (Figs. 8a,c,e). As the water gets shallower and the slope steeper, the phase lag of the incoming component calculated from the partial reflection approach and the phase lag of the Bessel incoming wave diverge (Figs. 8b,d,f). This shows that the inclusion of partial reflections (in our approach), introduces a large phase lag close to the shoreline in steep slope cases. Therefore, decomposing the standing wave into one single incoming wave and one single outgoing component as we did in Eq. (19), leads to an overestimation of the amplitude at the shoreline because the phase lags introduced by partial reflection are not accounted for. Therefore, in shallow water and steep slope cases, the standing solution cannot be decomposed into one incoming and one outgoing wave but is instead a combination of incoming waves (reflecting at each depth variation) and their corresponding outgoing waves, as represented in Fig. 1.

Second, we compare the Bessel incoming solution to Green's law (Figs. 8a,c,e, red and green lines). Both approaches assume no partial reflection. However, close to the shoreline, the solutions diverge, and the amplitude based on Green's law is larger than the amplitude based on Bessel solutions.

Using Bessel asymptotic expansions of J_0 and Y_0 (Friedrichs 1948; Lamb 1932), we express an approximation of the

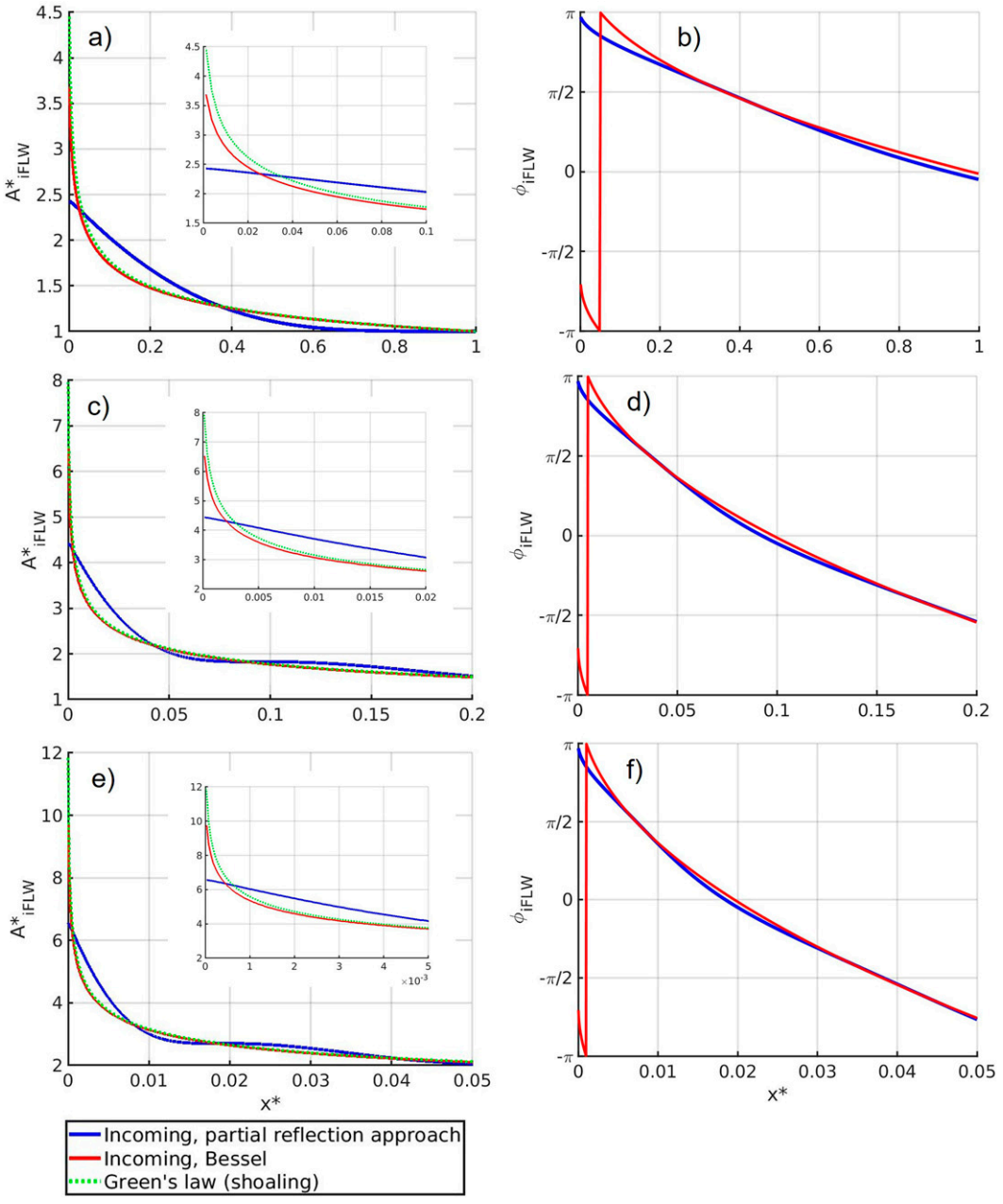

FIG. 8. Theoretical nondimensional incoming FLW (a),(c),(e) amplitudes and (b),(d),(f) phase for plane sloping bottom, comparing predictions from our partial reflection approach with Bessel function solutions and Green's law, for $f = 0.005$ Hz and three values of β: 0.05, 0.005, and 0.001. The shoreline is at $x^* = 0$. Panels (a), (c), and (e) include a zoom insert on small values of x^*.

amplitude of the incoming (and outgoing) wave, valid at large x (Guza and Bowen 1976), as a function of h:

$$A_{i/o\mathrm{FLW,Bessel,expansion}} \propto \sqrt{\frac{2}{\pi}}\left(\frac{g\beta}{\omega^2 x}\right)^{0.25} = \sqrt{\frac{2}{\pi}}\left(\frac{g\beta^2}{\omega^2 h}\right)^{0.25} = \sqrt{\frac{2}{\pi}}\left(\frac{g\beta^2}{\omega^2}\right)^{0.25} h^{-0.25}. \quad (21)$$

This expression is in $h^{-0.25}$. Therefore, for large x, the amplitude reduces to Green's law (shoaling) as was demonstrated by Synolakis (1991). This shows that Green's law is not an exact solution to the shallow water equations for small values of $2\sqrt{\omega^2 x/(g\beta)}$, even with the mild slope assumption. Indeed, the shoaling coefficient is calculated assuming sinusoidal waves and a flat bottom, while the solutions are in the form of Bessel functions over a sloping bottom.

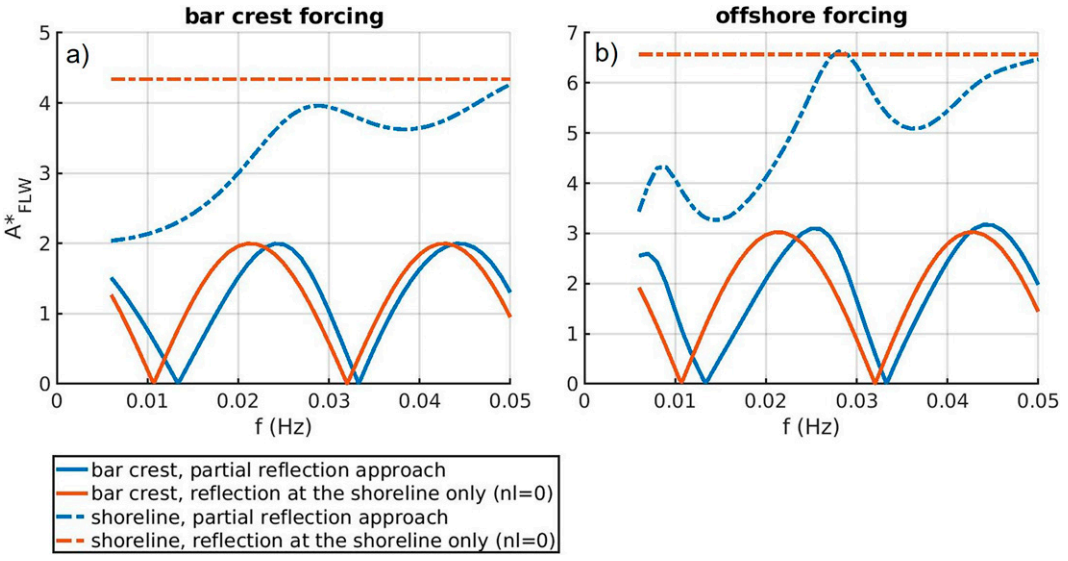

FIG. 9. Relative amplitude of the total FLW signal (A^*_{FLW}) for the realistic barred beach profile, comparing results from both the partial reflection approach and when reflection occurs only at the shoreline (nl = 0) for two locations, at the bar crest and at the shoreline. (a) Forcing at the bar crest, $dx^* = 0.004$, and (b) offshore forcing in 7-m depth, $dx^* = 0.0002$.

c. *Barred beach*

In appendix B, section b, we verified the validity of the partial reflection analytical approach using numerical modeling for a barred beach profile (Fig. B2). Here, we apply the partial reflection approach to the same barred beach profile to investigate the standing wave patterns arising from partial reflections and how the resulting wave amplitudes vary for different wave frequencies.

We calculate the amplitude of the FLWs for the barred beach case for two scenarios: 1) by assuming the incident FLWs originate at the bar crest location and 2) by assuming the incident FLWs originate seaward of the bar at 7-m depth. Comparison of these scenarios will show how the location where long waves are generated influences their amplitude in the surf zone. We plot the total amplitude as a function of the frequency (Fig. 9).

Over the barred profile, nodes and antinodes are expected at the bar crest for frequencies resonating with the geometry. The theoretical node frequencies, according to the theory without partial reflection, were given earlier in Eq. (13) by replacing x_{node} with the bar location x_{bar}, and antinodes frequencies are given by

$$f_{\mathrm{antinode}} = n\left(\int_{x_{\mathrm{bar}}}^{0} \frac{1}{\sqrt{gh}}\,dx\right)^{-1}. \tag{22}$$

For the barred beach bathymetry, based on Eqs. (13) and (22) the frequencies resonating at the bar crest are 0.010 Hz (node), 0.021 Hz (antinode), 0.032 Hz (node), and 0.043 Hz (antinode) representing the quarter-wave, half-wave, three-quarter-wave, and full-wave frequencies. As these predictions do not account for partial reflections (i.e., reflection is assumed to occur only at the shoreline), these frequencies coincide with where the level 0 minima and maxima are located in Fig. 9 (orange solid lines). However, as in the slope case (appendix B, section a) when partial reflections are included, the nodes and antinodes are shifted toward higher frequencies: 0.0130, 0.0240, 0.0325, and 0.0450 Hz (Fig. 9, blue solid lines).

At the shoreline, when partial reflections are not included, the total FLW amplitude does not vary with the frequency. Partial reflections introduce a local maximum ($f = 0.028$ Hz) and a local minimum ($f = 0.0036$ Hz) for cases where the FLWs are assumed to originate at both the bar crest (Fig. 9a) and offshore at 7 m depth (Fig. 9b).With the complete bathymetry profile included when the FLWs originate from offshore (Fig. 9b), there is an additional maximum ($f = 0.008$ Hz) and an additional minimum ($f = 0.0015$ Hz). The local extrema are also more pronounced in this latter case.

Standing wave patterns and resonance on a barred beach were studied by Symonds and Bowen (1984). We find very similar patterns (Fig. 9) compared to their study of breakpoint-forced long waves on a barred beach (refer to Fig. 4 in their study). Symonds and Bowen (1984) used Bessel solutions, therefore accounting for partial reflections. Our results show that similar resonance patterns at the shoreline are found without including breakpoint-forced outgoing FLWs and that the standing wave patterns at the shoreline originate from the presence of partial reflection, which are enhanced by the presence of the sandbar. We also note that the barred profile chosen by Symonds and Bowen (1984) was idealized, and the very shallow bar crest they considered led to a more pronounced oscillating pattern at the shoreline than with the realistic bathymetry profile we use here.

d. *Reef*

Reef geometries are known to amplify long waves due to resonance when the forcing matches the natural frequencies

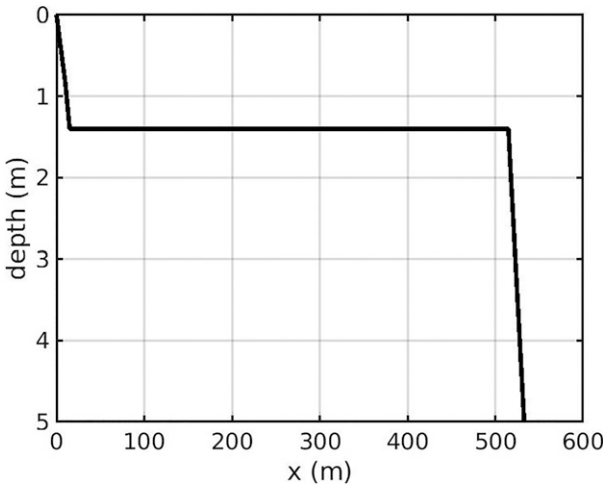

FIG. 10. Cross-reef bathymetry profile for a fringing reef based on the study by Buckley et al. (2018).

associated with standing wave motions over a reef bathymetry profile (Buckley et al. 2018). Here we show how partial reflections occurring both over forereef slope and beach slope affect the standing wave pattern associated with a reef geometry. The geometry adopted for the reef is borrowed from the study by Buckley et al. (2018), where at field scale, the forereef slope is 1/5 followed by a 500 m flat at 1.4-m depth then a beach with a 1/12 slope (Fig. 10). First, the calculations are done for a case where the incident FLWs originate from offshore of the reef crest on the fore reef at $h = 2$ m.

We calculate the amplitude for long waves with frequencies between 0.001 and 0.05 Hz, which includes very low frequencies (VLF, 0.001 to 0.005 Hz), that have been found to be resonant for reef studies with comparable geometries (Péquignet et al. 2009; Torres-Freyermuth et al. 2012; Cheriton et al. 2016; Gawehn et al. 2016; Buckley et al. 2018). The amplitude at the shoreline and at the reef crest follows a standing wave pattern set by the bathymetry profile (Fig. 11a). The frequencies where amplitude minima occur at the reef crest correspond to amplitude maxima at the shoreline, as the phase is shifted by 180° when outgoing waves reflect on the reef crest. In addition, the amplitude at the shoreline also depends on reflections over the beach slope, as the amplitude increases when the frequency increases (and the normalized slope β_{norm} gets milder), as shown in appendix B, section a. In the absence of partial reflections, the amplitude at the shoreline is constant with varying frequency (Fig. 11a, orange dash–dot line), consistent with the plane sloping beach case (Fig. 6) and the barred beach case (Fig. 9). The partial reflections introduce variations of the amplitude at the shoreline. The amplitude decreases as the frequency decreases (Fig. 11a, blue dash–dot line) to the point that the beach slope is not "seen" by the VLF waves

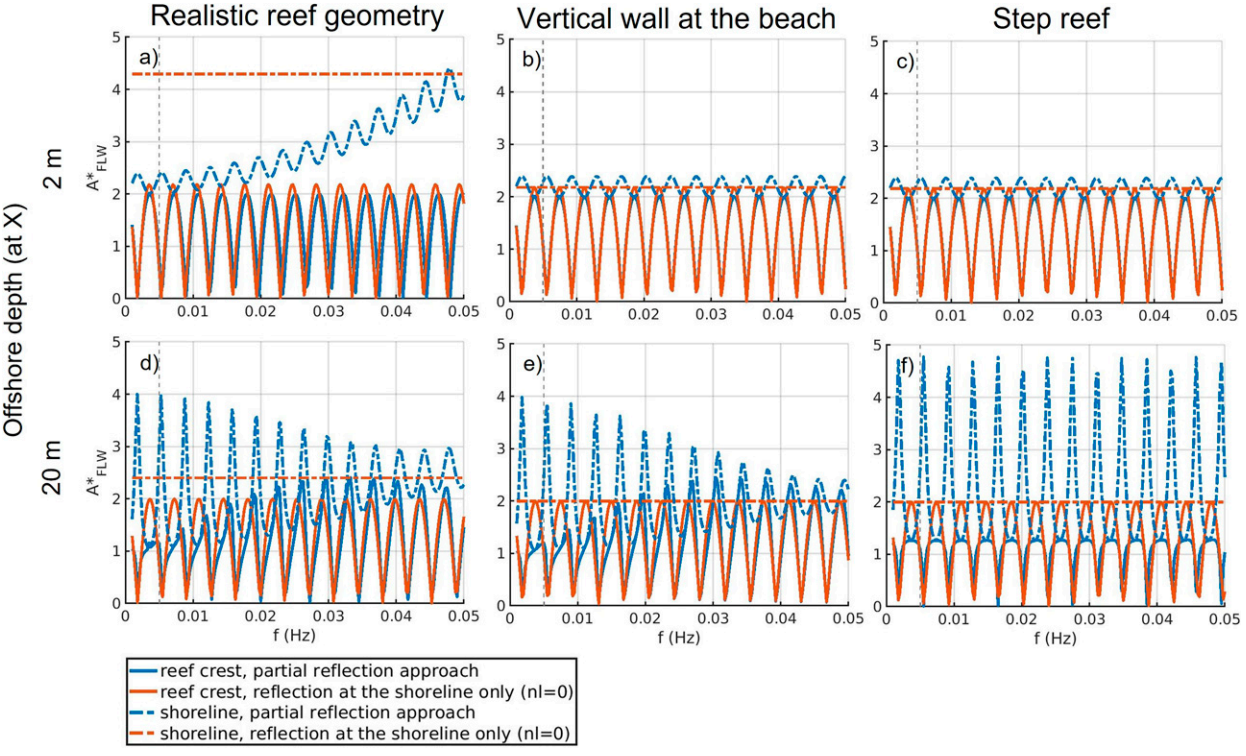

FIG. 11. Relative amplitude of the total FLW signal (A^*_{FLW}) for reef profiles, comparing results from both the partial reflection approach and when reflection occurs only at the shoreline (nl = 0) for two locations, at the reef crest and at the shoreline. (a),(d) Realistic reef geometry; (b),(e) modified reef geometry (vertical wall at the beach only); (c),(f) step reef; (top) offshore depth 2 m; (bottom) offshore depth 20 m, $dx^* = 0.0005$. The vertical dashed gray lines indicate the limit between VLF (<0.005 Hz) and IG frequencies (>0.005 Hz).

(<0.005 Hz). Therefore, the VLF waves effectively respond as if the reef geometry consists of a large single step (the reef crest) followed by a wall (the beach), while the beach slope only influences the shorter long waves and their amplitude at the shoreline is larger. At the reef crest (Fig. 11a, solid line), the nodes and antinodes are shifted toward higher frequencies as in the plane sloping beach (Fig. 6) and barred beach (Fig. 9) cases.

To further illustrate the role of varying beach slope, we consider a second case where the beach slope is replaced with a vertical wall (Fig. 11b). The increase of the amplitude at the shoreline with frequency for the original case with the beach slope (Fig. 11a, dash–dot blue line) is not present when the beach slope is replaced by a vertical wall (Fig. 11b, dash–dot blue line), confirming that the beach slope was responsible for the frequency dependency of the amplitude at the shoreline. The shift in the node and antinode frequencies disappears, as it is associated with the partial reflections on the beach slope.

A third case is also investigated where both the beach slope and forereef slope are replaced with vertical walls (referred to as the step reef case) (Fig. 11c). The results are very similar, whether the forereef slope is vertical or not, showing the forereef slope has minimal effect on the amplitude of long waves generated in water not much deeper (2 m here) than the reef flat (1.4 m deep).

We finally investigate the effect of offshore source depth of free long wave generation by reexamining the same three cases where the offshore depth is $h = 20$ m (Figs. 11d–f), while still normalizing the wave amplitude with the amplitude at 2 m, as using a consistent amplitude to normalize allows for a direct comparison of the magnitudes of amplitudes across both of these source depth scenarios. For this deeper source depth, with vertical walls both at the beach and at the forereef, the amplitude maxima (antinodes) at the shoreline attain larger values than when the offshore source depth is 2 m, because the reflection of the outgoing wave at the forereef is stronger (Figs. 11c,f). When the beach slope is vertical but the forereef slope is not (Fig. 11e), the amplitudes of the VLF waves at the shoreline are not substantially affected by the forereef slope, but as the frequency increases, the amplitude of the maxima (antinodes) decreases and the amplitude of the minima (nodes) increases (Fig. 11e, blue dash–dot line) because the resonance becomes milder with relatively milder forereef slope. The antinodes at the reef crest (Fig. 11e, solid blue line) are shifted toward higher frequency due to the horizontal extent of the forereef slope (which extends the reef flat width). When the beach slope is not vertical (Fig. 11d), there is a slight increase of shoreline amplitudes at higher frequencies compared with the case when the beach slope is vertical (Fig. 11e), but this is not as clear as in the case when the offshore depth is 2 m (Fig. 11a). Therefore, with deep offshore source depth, the beach slope tends to appear as a wall for most long waves, i.e., the differences of shoreline amplitudes between the more realistic reef geometry case with slopes (Fig. 11d) and the case with a vertical wall at the beach (Fig. 11e) are small. For real applications, this implies that the generation depth of free waves is important for the long-wave features over the reef.

Overall, our model shows that the resonance of high-frequency long waves is affected by the beach slope and the forereef slope as they propagate over a reef geometry. When the long-wave frequency corresponds to a node (antinode) at the reef crest, the amplitude over the reef flat is large (small). The beach slope reduces the amplitude of the long waves in the IG band (from 0.005 to 0.05 Hz) but does not affect the amplitude of the VLF waves, as the beach slope appears "transparent" to them. Thus, the VLF amplitudes remain large at resonant frequencies, providing a sensible explanation for why field studies have observed VLF waves to have higher amplitudes over the reef flat than higher-frequency long waves (Péquignet et al. 2014; Gawehn et al. 2016).

e. *Long-wave dissipation*

For the plane sloping beach case (section 4b), the free long waves are assumed to conserve energy and thus reach the shoreline without any dissipation. However, in reality, a proportion of the long waves dissipate before reaching the shoreline. The total reflection coefficient has thus been used as a proxy in measurements to estimate long-wave dissipation depth (e.g., de Bakker et al. 2014; van Dongeren et al. 2007). Since there is dissipation of energy, the outgoing signal is smaller than the incoming signal and the reflection coefficient is <1. This can be modeled (assuming total dissipation) by calculating the reflection coefficients over a section of slope, ending before the shoreline, as in appendix B, section c. The shallowest depth of the section serves as a proxy for the long-wave dissipation depth ($h_{d,\mathrm{LW}}$), since no local reflection occurs shoreward of this depth.

We consider a broad range of normalized slopes and frequencies. The reflection coefficients are plotted against the long-wave normalized bed slope:

$$\beta_{\mathrm{norm,LW}} = \frac{\beta}{\omega}\sqrt{\frac{g}{h_{d,\mathrm{LW}}}}, \tag{23}$$

which differs from β_{norm} [Eq. (17)], as it refers to the depth where long waves dissipate rather than the depth where short waves break. The reflection coefficients calculated as a function of $\beta_{\mathrm{norm,LW}}$ collapse onto a single curve (Fig. 12); thus, $\beta_{\mathrm{norm,LW}}$ and R^2 are highly correlated with a correlation coefficient of 0.95. The reflection coefficient consistently increases sublinearly with $\beta_{\mathrm{norm,LW}}$, for a range of long-wave dissipation depths and slopes, showing the relevance of the normalized bed slope [Eq. (17)] for estimating reflection when the dissipation is confined to occur a specific location, i.e., as can be done when dissipation is due to depth-limited breaking.

The total reflection of waves on a slope is dependent on the rate of energy dissipation, including depth-induced breaking, that occurs shoreward of the observation location (Battjes 1974). The surf similarity parameter (Battjes 1974) or Iribarren number (Iribarren Cavanilles and Casto Nogales 1949) is a commonly used breaking criterion, which is defined as the ratio of bed slope on the square root of wave steepness:

$$\xi = \frac{\beta}{\sqrt{H/L_0}}, \tag{24}$$

where H is a reference wave height, which can be taken as the offshore wave height or the breaking wave height, and L_0 is

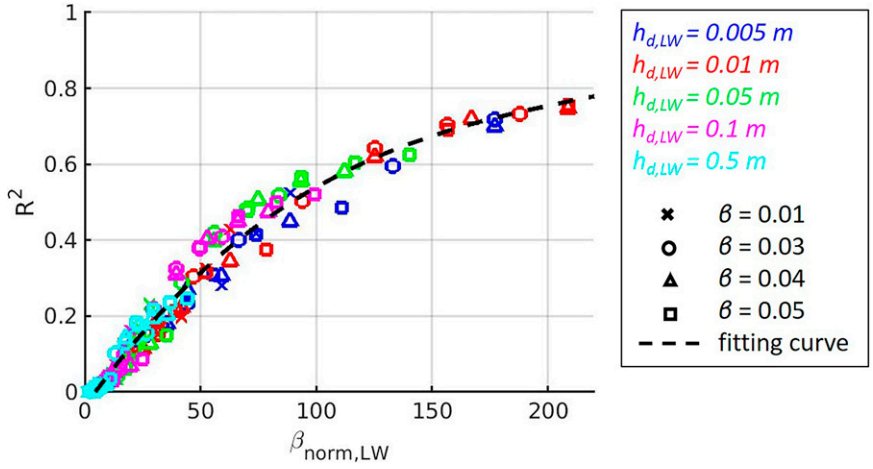

FIG. 12. Energy flux reflection coefficients (R^2) calculated at the offshore reference location ($x^* = 1$), as a function of the long-wave normalized bed slope ($\beta_{norm,LW}$) for a series of cases with five different bed slopes (β between 0.01 and 0.05) and long-wave dissipation depths ($h_{d,LW}$ between 0.005 and 0.5 m) for frequencies between 0.005 and 0.05 Hz.

the deep-water wavelength. As the breaking depth controls the reflection coefficient, the Iribarren number may be considered to parameterize predictions of the reflection coefficient (Battjes 1974; Miche 1951). However, such an approach does not consider the role of partial reflections, and as shown by Guedes et al. (2013), the Iribarren number does not collapse R^2 based on data collected on a dissipative beach (Raglan, New Zealand). In contrast, these present results, accounting for the effect of partial reflections, show that the normalized bed slope $\beta_{norm,LW}$ collapses all of the R^2 data (Fig. 13).

These results indicate that the relationship between long-wave reflection coefficients and $\beta_{norm,LW}$ can be used to help interpret surf-zone observations for cases where the cross-shore bathymetry profile is known and long-wave breaking is the dominant long-wave dissipation mechanism [e.g., as in the field sites studied by de Bakker et al. (2014)], with such observations of reflection coefficients enabling long-wave breaking depths (related to $h_{d,LW}$) to be estimated. This is illustrated using an example based on the barred beach profile considered earlier (Fig. B2). In Fig. 13, we calculate the long-wave dissipation depth as a function of the energy flux reflection coefficient, for five different frequencies, for monochromatic long waves generated at the bar crest. We find that the reflection coefficient is generally larger for both lower-frequency long waves and shallower breaking depths. At higher frequencies, the reflection coefficient is low unless the long waves break in very shallow water (<20 cm), indicating that high reflection coefficients would be reached only if the waves were breaking very close to the shoreline.

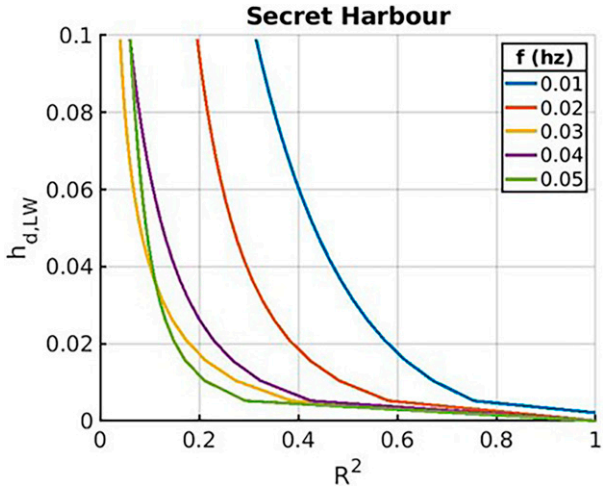

FIG. 13. Predicted long-wave dissipation depth ($h_{d,LW}$) vs energy flux reflection coefficient (R^2) at $h = 1.36$ m (bar crest), for five frequencies based on the barred beach bathymetry profile (Secret Harbour beach) in Fig. B2.

We note that these calculations provide an idealized representation of how long waves would be dissipated in natural surf zones (i.e., by assuming monochromatic waves and complete dissipation occurring at a specific cross-shore location). In reality, bulk reflection coefficients measured on a natural beach would be representing a range of long-wave frequencies and amplitudes. Therefore, at this stage this approach would only provide a rough estimation of the breaking depth, and thus here aims to simply demonstrate the concept, with further investigation required to calculate reflection coefficients for spectral long waves with partial dissipation.

In a relevant field study on two beaches, de Bakker et al. (2014) found, in agreement with Battjes et al. (2004) and van Dongeren et al. (2007), that high-frequency long waves were mostly dissipated while low-frequency long waves were strongly reflected and therefore any breaking of these waves would have to occur in very shallow water. In the present study, we show that the reflection coefficient is generally greater for low-frequency long waves than for high-frequency long waves, even if they break at the same location. It is also greater for shallower breaking depth, consistent with

Elgar et al. (1994), who observed a decrease in reflection coefficient with increasing wave height.

f. Limitations and possible extensions of the study

In this study we proposed an approach to investigate the propagation and reflection of monochromatic free long waves over arbitrary bathymetry profiles based on the linearized shallow-water equations in one dimension. The objective of the study was to show how long-wave amplitude and phase relationships are affected by continuous reflections over depth variations in the nearshore after FLWs are generated. To isolate the response of these processes, we needed to exclude other processes from the model. To obtain a complete description of the entire range of nearshore hydrodynamic processes, the role of other processes such as bottom friction, nonlinear transfers of energy, depth-limited breaking would need to be considered, in the way they are accounted for in numerical hydrodynamic models. However, to isolate the specific role of partial reflections, we did not include other processes in the model.

Nonlinearity is thus not accounted for, which can include energy transfers from and to short-wave frequencies and self interactions (van Dongeren et al. 2007). However, studies have found these nonlinear processes might not be dominant in the inner surf zone region (shoreward of short-wave breaking) once FLWs have been generated (de Bakker et al. 2014; Ruju et al. 2012).

The current study has focused on the propagation and reflection of FLWs in one (cross-shore) dimension only. In two (horizontal) dimensions, the solutions to the shallow water equation (Ursell 1952; Guza and Davis 1974) are trapped edge waves, which are refracted and reflected back to shallow water by the increasing water depth (Guza and Davis 1974; Eckart 1951; Chao and Pierson 1972). While an extension of our study to two dimensions would not be straightforward, it would also likely bring insight on how the propagation and reflection of long waves influence the amplitude and patterns of edge waves.

Last, this present study is of particular interest for long waves, as it has helped elucidate key features of long waves in the nearshore; for example, explaining why with reflection, the bed slope appears relatively steeper to low-frequency waves than short waves. However, we note that the approach is readily adaptable to short-wave (wind-sea and swell) reflections.

5. Conclusions

In this study we developed a new analytical solution to the linearized shallow water equations, based on energy conservation at each step of a discretized arbitrary bathymetry profile, which includes the incoming and outgoing components of the solution. This novel approach explicitly accounts for partial reflections and can therefore provide improved insight into the role of reflections on long-wave dynamics in the nearshore. By validating and then applying the approach, we demonstrated that, in the absence of dissipation, standing long waves in the surf zone are composed of a combination of incoming and outgoing waves lagging each other because of the continuous occurrence of partial reflections over depth variations. The role of phase lags is essential as they modify the amplitude of the waves and shift the location of standing nodes. The combination of multiple time-lagged incoming and outgoing waves can help explain why Green's law is not applicable to calculate the amplitude of free waves in very shallow water. The approach can also explain why the Bessel standing solution for long waves propagating over a steep slope cannot be decomposed into a single incoming wave and single outgoing wave but is instead a combination of smaller phase-lagged incoming and outgoing waves that reflect at each incremental depth variation.

Through extension of the approach to cases where long-wave dissipation occurs at a shallow inshore location (e.g., due to depth-limited breaking), we show how the long-wave normalized bed slope can explain variations of the total reflection coefficient for long waves propagating over a range of beach slopes and for different dissipation depths. Due to the dependency of the total reflection on long-wave dissipation, we also show how accounting for partial reflections can alternatively be used to estimate long-wave breaking depths from measurements of reflection coefficients.

This partial reflection approach provides insight and interpretation of previously observed shoreline processes (Lara et al. 2010; Baldock 2006), including partial standing patterns expected at the shoreline on barred beaches from breakpoint forcing theory (Symonds et al. 1982) and resonance features of low-frequency waves observed on reefs (Péquignet et al. 2014; Gawehn et al. 2016). Given the relationship between the amplitude of long waves and the shoreline wave runup, further extension of this method would also provide additional insight into the dynamics of low-frequency contributions to runup.

Acknowledgments. This research was funded by the Bluelink Partnership: a collaboration between the Australian Department of Defence, Bureau of Meteorology and CSIRO, and by the University of Western Australia.

Data availability statement. No data were used.

APPENDIX A

Background: Wave Reflection over a Single Step

By building on existing theory, summarized here, for predicting local reflection and transmission coefficients (Dean 1964) for a free long wave incident to a single depth variation (i.e., a step), we will develop theory in section 3 for analytical predictions over arbitrary cross-shore bathymetry profiles. As we are focusing on the propagation of long waves in the nearshore, we assume linear shallow water wave propagation, where the phase speed is $c = \omega/\kappa = \sqrt{gh}$, where ω is the angular frequency ($=2\pi f$, with f the ordinary frequency), κ is the wavenumber and h is the local water depth.

For a free wave propagating over a step depth variation, the local reflection and transmission coefficients must satisfy

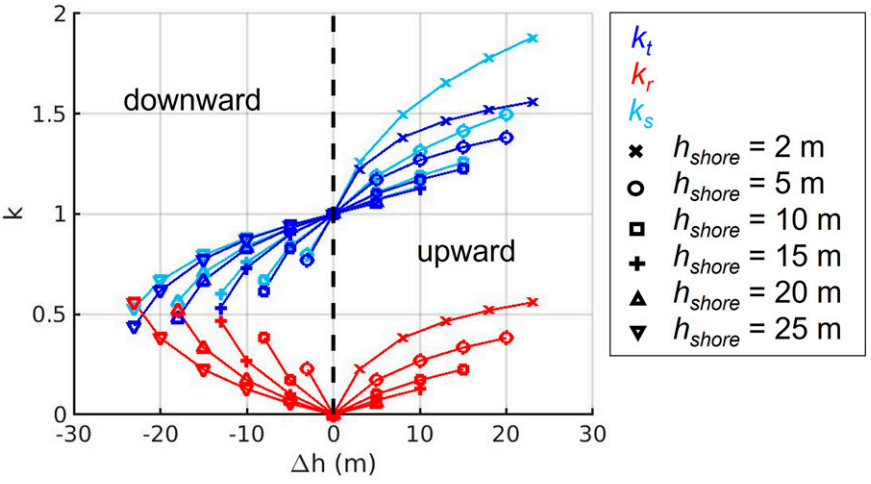

FIG. A1. Reflection (k_r), transmission (k_t), and shoaling (k_s) coefficients as a function of different step heights (Δh) for different reference depths on the shoreward side of the step (h_{shore}).

conservation of energy requirements, such that energy fluxes are conserved at the step (Bender and Dean 2003):

$$E_i c_{\text{sea}} - E_r c_{\text{sea}} = E_t c_{\text{shore}} \quad \text{or}$$
$$(A_i^2 - A_r^2) c_{\text{sea}} = A_t^2 c_{\text{shore}}, \tag{A1}$$

where A is the wave amplitude, $E = 1/2\rho g A^2$ is the energy density, the subscript i refers to the incident wave, the subscript r to the reflected wave, the subscript t to the transmitted wave, the subscript "sea" to the seaward side of the step (i.e., where the incident wave originates) and the subscript "shore" to the shoreward side of the step.

For a free long wave propagating over a step at a cross-shore location $x = x_0$, where x is the cross-shore coordinate (positive offshore) with $x = 0$ defined at the shoreline, for given depths h_{sea} and h_{shore} on the seaward and shoreward sides of the step, respectively, both the surface elevation and momentum must be continuous functions at all times t, such that

$$\zeta_i(x_0,t) + \zeta_r(x_0,t) = \zeta_t(x_0,t) \quad \text{and}$$
$$M_i(x_0,t) + M_r(x_0,t) = M_t(x_0,t), \tag{A2}$$

where ζ is the surface elevation and M is the momentum.

The elevations for harmonic incident, reflected and transmitted waves, respectively, have the form

$$\zeta_i(x,t) = A_i \exp\{i[\kappa_{\text{sea}}(x - x_0) + \omega t]\} + *,$$
$$\zeta_r(x,t) = A_r \exp[\kappa_{\text{sea}}(x - x_0) - \omega t + \phi] + *,$$
$$\zeta_t(x,t) = A_t e\{i[\kappa_{\text{shore}}(x - x_0) + \omega t]\} + *. \tag{A3}$$

where ϕ is the local phase difference between the incident and reflected wave. In Eq. (A3) the * denotes the complex conjugate of the preceding term, which will be dropped for brevity. By assuming linear shallow water wave propagation, small amplitude waves ($\zeta \ll h$) and with $M = \rho h U$ (Schäffer 1993; Contardo et al. 2021), the momentum of the waves is:

$$M_i(x,t) = \frac{\rho g h_{\text{sea}} \kappa_{\text{sea}}}{\omega} A_i \exp\{i[\kappa_{\text{sea}}(x - x_0) + \omega t]\}$$
$$= \rho c_{\text{sea}} A_i \exp\{i[\kappa_{\text{sea}}(x - x_0) + \omega t]\},$$
$$M_r(x,t) = -\frac{\rho g h_{\text{sea}} \kappa_{\text{sea}}}{\omega} A_r \exp\{i[\kappa_{\text{sea}}(x - x_0) - \omega t + \phi]\}$$
$$= -\rho c_{\text{sea}} A_r \exp\{i[\kappa_{\text{sea}}(x - x_0) - \omega t + \phi]\},$$
$$M_t(x,t) = \frac{\rho g h_{\text{shore}} \kappa_{\text{shore}}}{\omega} A_t \exp\{i[\kappa_{\text{shore}}(x - x_0) + \omega t]\}$$
$$= \rho c_{\text{shore}} A_t \exp\{i[\kappa_{\text{shore}}(x - x_0) + \omega t]\}. \tag{A4}$$

By applying continuity of surface elevation at the step [Eq. (A2)] at $t = 0$, we obtain

$$A_i + A_r e^{i\phi} = A_t \quad \text{and}$$
$$c_{\text{sea}}(A_i - A_r e^{i\phi}) = c_{\text{shore}} A_t \quad , \tag{A5}$$

which gives expressions for the reflection (k_r) and transmission (k_t) coefficients:

$$k_r = \frac{A_r e^{i\phi}}{A_i} = \frac{c_{\text{sea}} - c_{\text{shore}}}{c_{\text{shore}} + c_{\text{sea}}} = \frac{\kappa_{\text{shore}} - \kappa_{\text{sea}}}{\kappa_{\text{shore}} + \kappa_{\text{sea}}} \quad \text{and} \tag{A6}$$

$$k_t = \frac{A_t}{A_i} = \frac{2c_{\text{sea}}}{c_{\text{shore}} + c_{\text{sea}}} = \frac{2\kappa_{\text{shore}}}{\kappa_{\text{shore}} + \kappa_{\text{sea}}}. \tag{A7}$$

We note that Eq. (A5) is consistent with Eq. (A1) when either $\phi = 0$ or π. If $\phi = 0$, $A_t > A_i$ (representing upward propagation) and if $\phi = \pi$, $A_t < A_i$ (representing downward propagation). Therefore, if $c_{\text{shore}} < c_{\text{sea}}$ (equivalent to $h_{\text{shore}} < h_{\text{sea}}$, i.e., shallower shoreward), $k_t > 1$ so the transmitted wave is larger than the incident wave and k_r is positive so $\phi = 0$. If $c_{\text{shore}} > c_{\text{sea}}$ ($h_{\text{shore}} > h_{\text{sea}}$, i.e., a deeper depth shoreward), $k_t < 1$, implying that the transmitted wave is smaller than the incident wave and k_r is negative such that the reflected wave is in antiphase with the incident wave ($\phi = \pi$).

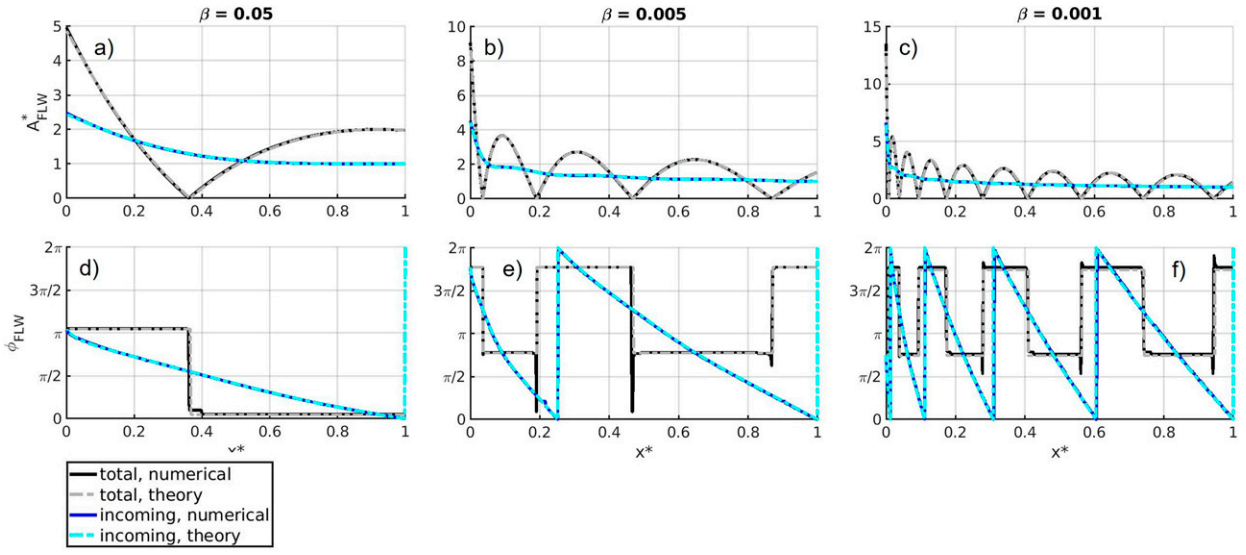

FIG. B1. Comparison of the partial reflection analytical approach and numerical model results for predictions of the (top) normalized amplitude and (bottom) phase lag of the FLW (referenced to the incoming FLW at $x^* = 1$) as a function of the dimensionless cross-shore distance $x^* = x/X$, for $\beta = 0.05, 0.005, 0.001$, with $X = 2000$ m.

For long waves in shallow water, the phase speed is only a function of the local water depth, therefore,

$$k_r = \frac{\sqrt{h_{\text{sea}}} - \sqrt{h_{\text{shore}}}}{\sqrt{h_{\text{shore}}} + \sqrt{h_{\text{sea}}}} \quad \text{and} \tag{A8}$$

$$k_t = \frac{2\sqrt{h_{\text{sea}}}}{\sqrt{h_{\text{shore}}} + \sqrt{h_{\text{sea}}}}. \tag{A9}$$

Note that if reflection is neglected in Eq. (A1), we obtain

$$k_{s=}\frac{A_t}{A_i} = \sqrt{c_{\text{sea}}/c_{\text{shore}}} = (h_{\text{sea}}/h_{\text{shore}})^{0.25}, \tag{A10}$$

which is the shoaling coefficient (i.e., Holthuijsen 2007). If the depth variation across the step is small, reflections may be neglected (Koh and Le Méhauté 1966; Svendsen and Hansen 1977), while in steep slope cases, they become important.

To illustrate how the local reflection, transmission and shoaling coefficients vary for steps with different depths, we show responses for both upward and downward propagating long waves with depth differences varying between 2 and 25 m (Fig. A1). For the same depth difference, reflections in both directions have the same value, as the reflected wave propagates at the same depth as the incident wave. For small depth variations, the local reflection coefficient is small, which justifies neglecting reflection in those cases. For large depth variations (i.e., $|\Delta h| > \sim 20$ m), the downward reflection coefficient reaches values > 0.5 and is larger than the transmission coefficient. The transmission coefficient is >1 in the upward direction and <1 in the downward direction of the effect of shoaling. The transmission coefficient is smaller than the shoaling coefficient, as not all the energy is transmitted when reflection is taken into account.

APPENDIX B

Verification Using Numerical Modeling

a. Plane sloping beach

We next verify our approach by comparing the results with those of a numerical model, forced with a monochromatic long wave. We use a one-dimensional numerical model (Contardo et al. 2021), which solves the linearized depth-integrated mass and momentum conservation equations, averaged over short-wave periods:

$$\frac{\partial \zeta}{\partial t} + \frac{\partial (hU)}{\partial x} = 0,$$
$$\frac{\partial U}{\partial t} + g\frac{\partial \zeta}{\partial x} = 0. \tag{B1}$$

To verify our approach, the numerical model is run in the linear slope configuration, with three values of β: 0.05, 0.005, 0.001, at $f = 0.005$ Hz. We compare the amplitude of the FLWs and their phase lag (referenced to the initial amplitude and phase at $x^* = 1$) that are obtained using both the numerical model and the partial reflection analytical approach (Fig. B1). The numerical model is run for a duration of five wave periods, which was enough time to reach a steady state, and the amplitude measured is that of the last wave to propagate across the domain and back. The numerical model and partial reflection analytical approach are in very good agreement. The amplitude of the FLWs at the shoreline decreases as β increases, as the effect of partial reflections is stronger for steeper slope. The processes responsible for this trend are discussed in section 4a.

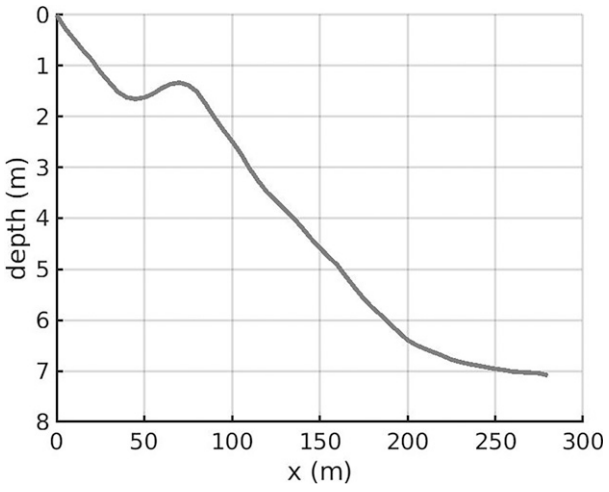

FIG. B2. Cross-shore profile of the barred beach bathymetry.

b. Complex bathymetry profile (barred beach)

Our partial reflection analytical model is further verified for a realistic bathymetry profile by comparing it with results from the numerical model. A barred beach geometry is taken as the longshore average (over 400 m) of a bathymetry survey (3 February 2014) of Secret Harbour beach in Western Australia (Contardo and Symonds 2013, 2015; Contardo et al. 2019). The 1.34-m-deep sandbar crest is located 70 m from the shoreline and the 1.65 m trough is located 45 m from the shore (Fig. B2). The reference (X = 70 m) is taken at the sandbar crest. We vary the frequency of the long wave and study the response.

Four frequencies are specifically considered, covering the range of frequencies of the infragravity wave spectrum and including frequencies with a node and an antinode at the bar crest: 0.005, 0.013, 0.024, and 0.05 Hz. Figure B3 presents the amplitudes, calculated both analytically (partial reflection approach) and modeled numerically, as a function of the cross-shore location for the four frequencies. The analytical and numerical model results are in very good agreement. The amplitude of the FLWs at the shoreline decreases as the wave frequency decreases. The processes responsible for this trend are discussed in section 4a and the standing patterns are discussed in section 4c.

c. Truncated plane beach (section of slope)

In the above examples, the slope ends at the shoreline. Therefore, the incoming wave is fully reflected. We now consider the case of a truncated plane beach, assuming an infinite flat plateau beyond the slope, where waves propagate indefinitely. This case is of interest because it could be a proxy in field observations where the long waves fully dissipate at a particular depth (i.e., no reflection occurs shoreward of this point), for example, due to long-wave breaking. We model, both analytically (using the partial reflection approach) and numerically, the propagation of a wave of frequency f = 0.005 Hz

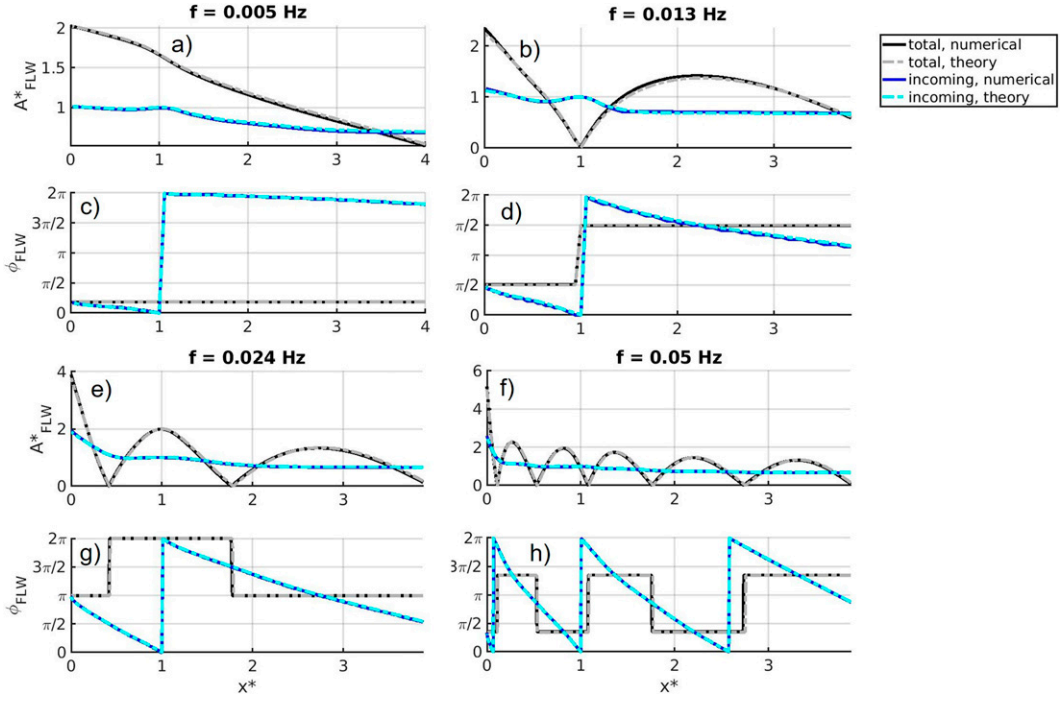

FIG. B3. Comparison of the partial reflection analytical approach and the numerical model results for the barred beach profile in Fig. B2, for predictions of the (a),(b),(e),(f) normalized amplitude and (c),(d), (g),(h) phase lag of the FLW (referenced to the incoming FLW at $x^* = 1$), calculated at four frequencies.

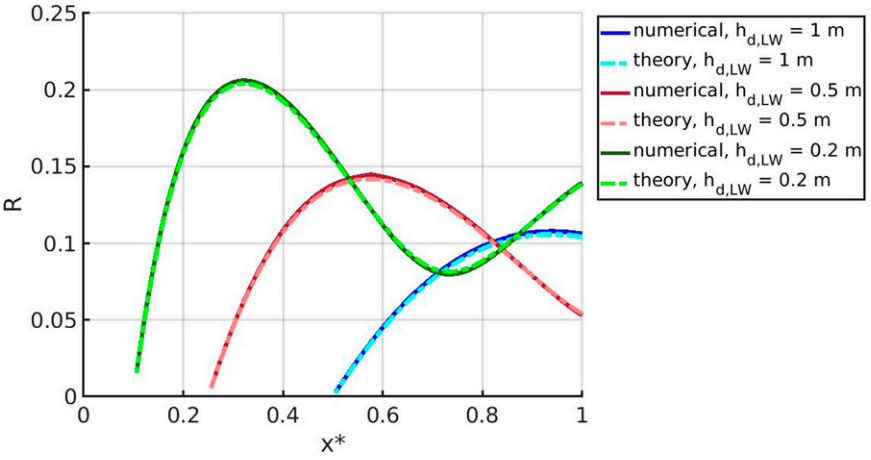

FIG. B4. Total reflection coefficient vs nondimensional cross-shore distance (shoreline at $x = 0$) for $f = 0.005$ Hz and $\beta = 0.005$, for a section of slope starting at $h = 5$ m and finishing at $h_{d,\mathrm{LW}} = 1$, 0.5, or 0.2 m.

over a slope with $\beta = 0.005$, with the initial offshore depth at 2 m and the inshore at a given cutoff (dissipation) depth for $h_{d,\mathrm{LW}}$, with three cutoff depths considered here ($h_{d,\mathrm{LW}} = 0.1$, 0.5 and 1 m). Thus, while in previous cases where the slope ended at the shoreline and the total reflection coefficient was by definition 1 at all cross-shore locations, here the total reflection coefficient is everywhere <1. We calculate this reflection coefficient [Eq. (8)] for both the analytical and numerical models and we find that both models are in excellent agreement (Fig. B4). In this example with a bottom depth of 5 m, the reflection coefficient reaches maxima of 0.21, 0.14, and 0.11 at $x^* = 0.32$, 0.58, and 0.94 for values of the cutoff depth of 0.2, 0.5 and 1 m, respectively, so that the maximum reflection coefficient is larger and located closer to the shore for long waves breaking close to the shoreline. Further analysis and discussion of reflection, associated with long-wave dissipation, are revisited in section 4e.

REFERENCES

Abdelrahman, S. M., 1986: Shore wave modulation due to infragravity waves in the nearshore zone, with applications. Ph.D. dissertation, Naval Postgraduate School, 128 pp.

Almar, R., A. Nicolae Lerma, B. Castelle, and T. Scott, 2018: On the influence of reflection over a rhythmic swash zone on surf zone dynamics. *Ocean Dyn.*, **68**, 899–909, https://doi.org/10.1007/s10236-018-1165-5.

Baldock, T. E., 2006: Long wave generation by the shoaling and breaking of transient wave groups on a beach. *Proc. Roy. Soc.*, **462**, 1853–1876, https://doi.org/10.1098/rspa.2005.1642.

Battjes, J. A., 1974: Surf similarity. *14th Int. Conf. on Coastal Engineering*, Copenhagen, Denmark, American Society of Civil Engineers, 466–480, https://icce-ojs-tamu.tdl.org/icce/article/view/1971/1464.

——, H. J. Bakkenes, T. T. Janssen, and A. R. van Dongeren, 2004: Shoaling of subharmonic gravity waves. *J. Geophys. Res.*, **109**, C02009, https://doi.org/10.1029/2003JC001863.

Bayındır, C., and S. Farazande, 2021: The solution of the long-wave equation for various nonlinear depth and breadth profiles in the power-law form. *Dyn. Atmos. Oceans*, **96**, 101254, https://doi.org/10.1016/j.dynatmoce.2021.101254.

Bender, C. J., and R. G. Dean, 2003: Wave transformation by two-dimensional bathymetric anomalies with sloped transitions. *Coastal Eng.*, **50**, 61–84, https://doi.org/10.1016/j.coastaleng.2003.08.002.

Bertin, X., K. Martins, A. Bakker, T. Chataigner, T. Guérin, T. Coulombier, and O. Viron, 2020: Energy transfers and reflection of infragravity waves at a dissipative beach under storm waves. *J. Geophys. Res. Oceans*, **125**, e2019JC015714, https://doi.org/10.1029/2019JC015714.

Bowen, A. J., and R. T. Guza, 1978: Edge waves and surf beat. *J. Geophys. Res.*, **83**, 1913–1920, https://doi.org/10.1029/JC083iC04p01913.

Buckley, M. L., R. J. Lowe, J. E. Hansen, A. R. Van Dongeren, and C. D. Storlazzi, 2018: Mechanisms of wave-driven water level variability on reef-fringed coastlines. *J. Geophys. Res. Oceans*, **123**, 3811–3831, https://doi.org/10.1029/2018JC013933.

Chao, Y.-Y., and W. J. Pierson, 1972: Experimental studies of the refraction of uniform wave trains and transient wave groups near a straight caustic. *J. Geophys. Res.*, **77**, 4545–4554, https://doi.org/10.1029/JC077i024p04545.

Cheriton, O. M., C. D. Storlazzi, and K. J. Rosenberger, 2016: Observations of wave transformation over a fringing coral reef and the importance of low-frequency waves and offshore water levels to runup, overwash, and coastal flooding. *J. Geophys. Res. Oceans*, **121**, 3121–3140, https://doi.org/10.1002/2015JC011231.

Contardo, S., and G. Symonds, 2013: Infragravity response to variable wave forcing in the nearshore. *J. Geophys. Res. Oceans*, **118**, 7095–7106, https://doi.org/10.1002/2013JC009430.

——, and ——, 2015: Sandbar straightening under wind-sea and swell forcing. *Mar. Geol.*, **368**, 25–41, https://doi.org/10.1016/j.margeo.2015.06.010.

——, ——, and F. Dufois, 2018: Breakpoint forcing revisited: Phase between forcing and response. *J. Geophys. Res. Oceans*, **123**, 1354–1363, https://doi.org/10.1002/2017JC013138.

——, ——, L. E. Segura, R. J. Lowe, and J. E. Hansen, 2019: Infragravity wave energy partitioning in the surf zone in

response to wind-sea and swell forcing. *J. Mar. Sci. Eng.*, **7**, 383, https://doi.org/10.3390/jmse7110383.

——, R. J. Lowe, J. E. Hansen, D. P. Rijnsdorp, F. Dufois, and G. Symonds, 2021: Free and forced components of shoaling long waves in the absence of short wave breaking. *J. Phys. Oceanogr.*, **51**, 1465–1487, https://doi.org/10.1175/JPO-D-20-0214.1.

de Bakker, A. T. M., M. F. S. Tissier, and B. G. Ruessink, 2014: Shoreline dissipation of infragravity waves. *Cont. Shelf Res.*, **72**, 73–82, https://doi.org/10.1016/j.csr.2013.11.013.

de Beer, A. F., R. T. McCall, J. W. Long, M. F. S. Tissier, and A. J. H. M. Reniers, 2021: Simulating wave runup on an intermediate–reflective beach using a wave-resolving and a wave-averaged version of XBeach. *Coastal Eng.*, **163**, 103788, https://doi.org/10.1016/j.coastaleng.2020.103788.

Dean, R. G., 1964: Long wave modification by linear transitions. *J. Waterw. Harbors Div.*, **90** (1), 1–29, https://doi.org/10.1061/JWHEAU.0000351.

Didenkulova, I., E. Pelinovsky, and T. Soomere, 2009: Long surface wave dynamics along a convex bottom. *J. Geophys. Res.*, **114**, C07006, https://doi.org/10.1029/2008JC005027.

Eckart, C., 1951: Surface waves on water of variable depth. Wave Rep. 100, 60 pp., http://resolver.tudelft.nl/uuid:ab1ada31-db80-4601-8911-b261f36c2198.

Elgar, S., T. H. C. Herbers, M. Okihiro, J. Oltman-Shay, and R. T. Guza, 1992: Observations of infragravity waves. *J. Geophys. Res.*, **97**, 15 573–15 577, https://doi.org/10.1029/92JC01316.

——, ——, and R. T. Guza, 1994: Reflection of ocean surface gravity waves from a natural beach. *J. Phys. Oceanogr.*, **24**, 1503–1511, https://doi.org/10.1175/1520-0485(1994)024<1503:ROOSGW>2.0.CO;2.

Fiedler, J. W., P. B. Smit, K. L. Brodie, J. McNinch, and R. T. Guza, 2018: Numerical modeling of wave runup on steep and mildly sloping natural beaches. *Coastal Eng.*, **131**, 106–113, https://doi.org/10.1016/j.coastaleng.2017.09.004.

——, A. P. Young, B. C. Ludka, W. C. O'Reilly, C. Henderson, M. A. Merrifield, and R. T. Guza, 2020: Predicting site-specific storm wave run-up. *Nat. Hazards*, **104**, 493–517, https://doi.org/10.1007/s11069-020-04178-3.

Friedrichs, K. O., 1948: Waves on a shallow sloping beach. *Commun. Pure Appl. Math.*, **1**, 109–134, https://doi.org/10.1002/cpa.3160010202.

Gawehn, M., A. van Dongeren, A. van Rooijen, C. D. Storlazzi, O. M. Cheriton, and A. Reniers, 2016: Identification and classification of very low frequency waves on a coral reef flat. *J. Geophys. Res. Oceans*, **121**, 7560–7574, https://doi.org/10.1002/2016JC011834.

Green, G., 1838: On the motion of waves in a variable canal of small depth and width. *Trans. Cambridge Philos. Soc.*, **6**, 457.

Guedes, R. M. C., K. R. Bryan, and G. Coco, 2013: Observations of wave energy fluxes and swash motions on a low-sloping, dissipative beach. *J. Geophys. Res. Oceans*, **118**, 3651–3669, https://doi.org/10.1002/jgrc.20267.

Guza, R. T., and R. E. Davis, 1974: Excitation of edge waves by waves incident on a beach. *J. Geophys. Res.*, **79**, 1285–1291, https://doi.org/10.1029/JC079i009p01285.

——, and A. J. Bowen, 1976: Resonant interactions for waves breaking on a beach. *Proc. 15th Conf. on Coastal Engineering*, Honolulu, HI, American Society of Civil Engineers, 560–579, https://icce-ojs-tamu.tdl.org/icce/article/view/3080/2745.

Henderson, S. M., and A. J. Bowen, 2002: Observations of surf beat forcing and dissipation. *J. Geophys. Res.*, **107**, 3193, https://doi.org/10.1029/2000JC000498.

——, R. T. Guza, S. Elgar, T. H. C. Herbers, and A. J. Bowen, 2006: Nonlinear generation and loss of infragravity wave energy. *J. Geophys. Res.*, **111**, C12007, https://doi.org/10.1029/2006JC003539.

Holthuijsen, L. H., 2007: *Waves in Oceanic and Coastal Waters*. Cambridge University Press, 387 pp.

Inch, K., M. Davidson, G. Masselink, and P. Russell, 2015: Propagation and dissipation of infragravity waves on a dissipative beach with energetic wave forcing. *The Proceedings of the Coastal Sediments 2015*, P. Wang, J. D. Rosati, and J. Cheng, Eds., World Scientific, 1–12, https://doi.org/10.1142/9789814689977_0071.

Iribarren Cavanilles, R., and M. Casto Nogales, 1949: Protection des ports. PIANC Rep., 50 pp., http://resolver.tudelft.nl/uuid:7ab718ff-a74d-4141-8c3f-413044c751c4.

Koh, R. C. Y., and B. Le Méhauté, 1966: Wave shoaling. *J. Geophys. Res.*, **71**, 2005–2012, https://doi.org/10.1029/JZ071i008p02005.

Lamb, H., 1932: *Hydrodynamics*. 6th ed. Dover Publications, 738 pp.

Lara, J. L., A. Ruju, and I. J. Losada, 2010: Reynolds averaged Navier-Stokes modelling of long waves induced by a transient wave group on a beach. *Proc. Roy. Soc.*, **A467**, 1215–1242, https://doi.org/10.1098/rspa.2010.0331.

Liao, Z., S. Li, Y. Liu, and Q. Zou, 2021: An analytical spectral model for infragravity waves over topography in intermediate and shallow water under nonbreaking conditions. *J. Phys. Oceanogr.*, **51**, 2749–2765, https://doi.org/10.1175/JPO-D-20-0164.1.

Longuet-Higgins, M. S., and R. W. Stewart, 1962: Radiation stress and mass transport in gravity waves, with application to 'surf beats'. *J. Fluid Mech.*, **13**, 481–504, https://doi.org/10.1017/S0022112062000877.

Madsen, O. S., and S. M. White, 1976: Reflection and transmission characteristics of porous rubble-mound breakwaters. CERC Misc. Rep. 76-5, U.S. Army Corps of Engineers, 138 pp., https://repository.tudelft.nl/islandora/object/uuid%3Ad82e594c-ed8c-4e18-b0fd-0ead288ad5a4.

Madsen, P. A., and D. R. Fuhrman, 2008: Run-up of tsunamis and long waves in terms of surf-similarity. *Coastal Eng.*, **55**, 209–223, https://doi.org/10.1016/j.coastaleng.2007.09.007.

Masselink, G., 1995: Group bound long waves as a source of infragravity energy in the surf zone. *Cont. Shelf Res.*, **15**, 1525–1547, https://doi.org/10.1016/0278-4343(95)00037-2.

Mei, C. C., 1989: *The Applied Dynamics of Ocean Surface Waves*. World Scientific Publishing, 768 pp.

——, and C. Benmoussa, 1984: Long waves induced by short-wave groups over an uneven bottom. *J. Fluid Mech.*, **139**, 219–235, https://doi.org/10.1017/S0022112084000331.

Merrifield, M. A., J. M. Becker, M. Ford, and Y. Yao, 2014: Observations and estimates of wave-driven water level extremes at the Marshall Islands. *Geophys. Res. Lett.*, **41**, 7245–7253, https://doi.org/10.1002/2014GL061005.

Miche, M., 1951: Le pouvoir réfléchissant des ouvrages maritimes exposés à l'action de la houle. *Ann. Ponts Chaussees*, **121**, 285–319.

Moura, T., and T. E. Baldock, 2017: Remote sensing of the correlation between breakpoint oscillations and infragravity waves in the surf and swash zone. *J. Geophys. Res. Oceans*, **122**, 3106–3122, https://doi.org/10.1002/2016JC012233.

——, and ——, 2019: The influence of free long wave generation on the shoaling of forced infragravity waves. *J. Mar. Sci. Eng.*, **7**, 305, https://doi.org/10.3390/jmse7090305.

Munk W. H., 1949: Surf beats. *Eos, Trans. Amer. Geophys. Union*, **30**, 849–854, https://doi.org/10.1029/TR030i006p00849.

Nielsen, P., 2017: Surf beat "shoaling." *Coastal Dynamics 2017*, Helsingor, Denmark, Coastal Dynamics Steering Committee, 443–450, http://coastaldynamics2017.dk/onewebmedia/198_Nielsen.pdf.

Okihiro, M., and R. T. Guza, 1995: Infragravity energy modulation by tides. *J. Geophys. Res.*, **100**, 16 143–16 148, https://doi.org/10.1029/95JC01545.

Padilla, E. M., and J. M. Alsina, 2017: Transfer and dissipation of energy during wave group propagation on a gentle beach slope. *J. Geophys. Res. Oceans*, **122**, 6773–6794, https://doi.org/10.1002/2017JC012703.

Péquignet, A. C. N., J. M. Becker, M. A. Merrifield, and J. Aucan, 2009: Forcing of resonant modes on a fringing reef during tropical storm Man-Yi. *Geophys. Res. Lett.*, **36**, L03607, https://doi.org/10.1029/2008GL036259.

——, ——, and ——, 2014: Energy transfer between wind waves and low-frequency oscillations on a fringing reef, Ipan, Guam. *J. Geophys. Res. Oceans*, **119**, 6709–6724, https://doi.org/10.1002/2014JC010179.

Pomeroy, A., R. Lowe, G. Symonds, A. Van Dongeren, and C. Moore, 2012: The dynamics of infragravity wave transformation over a fringing reef. *J. Geophys. Res.*, **117**, C11022, https://doi.org/10.1029/2012JC008310.

Quataert, E., C. Storlazzi, A. van Dongeren, and R. McCall, 2020: The importance of explicitly modelling sea-swell waves for runup on reef-lined coasts. *Coastal Eng.*, **160**, 103704, https://doi.org/10.1016/j.coastaleng.2020.103704.

Reniers, A. J. H. M., A. R. van Dongeren, J. A. Battjes, and E. B. Thornton, 2002: Linear modeling of infragravity waves during Delilah. *J. Geophys. Res.*, **107**, 3137, https://doi.org/10.1029/2001JC001083.

Roelvink, D., A. Reniers, A. van Dongeren, J. van Thiel de Vries, R. McCall, and J. Lescinski, 2009: Modelling storm impacts on beaches, dunes and barrier islands. *Coastal Eng.*, **56**, 1133–1152, https://doi.org/10.1016/j.coastaleng.2009.08.006.

Ruessink, B. G., 1998: Bound and free infragravity waves in the nearshore zone under breaking and nonbreaking conditions. *J. Geophys. Res.*, **103**, 12 795–12 805, https://doi.org/10.1029/98JC00893.

Ruju, A., J. L. Lara, and I. J. Losada, 2012: Radiation stress and low-frequency energy balance within the surf zone: A numerical approach. *Coastal Eng.*, **68**, 44–55, https://doi.org/10.1016/j.coastaleng.2012.05.003.

——, ——, and ——, 2014: Numerical analysis of run-up oscillations under dissipative conditions. *Coastal Eng.*, **86**, 45–56, https://doi.org/10.1016/j.coastaleng.2014.01.010.

Russell, P. E., 1993: Mechanisms for beach erosion during storms. *Cont. Shelf Res.*, **13**, 1243–1265, https://doi.org/10.1016/0278-4343(93)90051-X.

Schäffer, H. A., 1993: Infragravity waves induced by short-wave groups. *J. Fluid Mech.*, **247**, 551–588, https://doi.org/10.1017/S0022112093000564.

Seelig, W. N., and J. P. Ahrens, 1981: Estimation of wave reflection and energy dissipation coefficients for beaches, revetments, and breakwaters. U.S. Army Coastal Engineering Research Center Tech. Paper 81-1, 44 pp., https://erdc-library.erdc.dren.mil/jspui/bitstream/11681/25428/1/Technical%20Paper%20No%2081-1.pdf.

Sheremet, A., R. T. Guza, S. Elgar, and T. H. C. Herbers, 2002: Observations of nearshore infragravity waves: Seaward and shoreward propagating components. *J. Geophys. Res.*, **107**, 10-1–10-10, https://doi.org/10.21236/ADA409757.

Stockdon, H. F., R. A. Holman, P. A. Howd, and A. H. Sallenger, 2006: Empirical parameterization of setup, swash, and runup. *Coastal Eng.*, **53**, 573–588, https://doi.org/10.1016/j.coastaleng.2005.12.005.

Suhayda, J. N., 1974: Standing waves on beaches. *J. Geophys. Res.*, **79**, 3065–3071, https://doi.org/10.1029/JC079i021p03065.

Svendsen, I. A., and J. B. Hansen, 1977: The wave height variation for regular waves in shoaling water. *Coastal Eng.*, **1**, 261–284, https://doi.org/10.1016/0378-3839(77)90018-7.

Symonds, G., and A. J. Bowen, 1984: Interactions of nearshore bars with incoming wave groups. *J. Geophys. Res.*, **89**, 1953–1959, https://doi.org/10.1029/JC089iC02p01953.

——, D. A. Huntley, and A. J. Bowen, 1982: Two-dimensional surf beat: Long wave generation by a time-varying breakpoint. *J. Geophys. Res.*, **87**, 492–498, https://doi.org/10.1029/JC087iC01p00492.

Synolakis, C. E., 1991: Green's law and the evolution of solitary waves. *Phys. Fluids*, **3**, 490–491, https://doi.org/10.1063/1.858107.

Thomson, J., S. Elgar, B. Raubenheimer, T. H. C. Herbers, and R. T. Guza, 2006: Tidal modulation of infragravity waves via nonlinear energy losses in the surfzone. *Geophys. Res. Lett.*, **33**, L05601, https://doi.org/10.1029/2005GL025514.

Thornton, E. B., and R. T. Guza, 1982: Energy saturation and phase speeds measured on a natural beach. *J. Geophys. Res.*, **87**, 9499–9508, https://doi.org/10.1029/JC087iC12p09499.

Torres-Freyermuth, A., and Coauthors, 2012: Wave-induced extreme water levels in the Puerto Morelos fringing reef lagoon. *Nat. Hazards Earth Syst. Sci.*, **12**, 3765–3773, https://doi.org/10.5194/nhess-12-3765-2012.

Tucker, M. J., 1950: Surf beats: Sea waves of 1 to 5 min. period. *Proc. Roy. Soc.*, **202**, 565–573, https://doi.org/10.1098/rspa.1950.0120.

Ursell, F., 1952: Edge waves on a sloping beach. *Proc. Roy. Soc.*, **214**, 79–97, https://doi.org/10.1098/rspa.1952.0152.

——, R. G. Dean, and Y. S. Yu, 1960: Forced small-amplitude water waves: A comparison of theory and experiment. *J. Fluid Mech.*, **7**, 33–52, https://doi.org/10.1017/S0022112060000037.

van Dongeren, A., J. Battjes, T. Janssen, J. van Noorloos, K. Steenhauer, G. Steenbergen, and A. Reniers, 2007: Shoaling and shoreline dissipation of low-frequency waves. *J. Geophys. Res.*, **112**, C02011, https://doi.org/10.1029/2006JC003701.

——, R. Lowe, A. Pomeroy, D. M. Trang, D. Roelvink, G. Symonds, and R. Ranasinghe, 2013: Numerical modeling of low-frequency wave dynamics over a fringing coral reef. *Coastal Eng.*, **73**, 178–190, https://doi.org/10.1016/j.coastaleng.2012.11.004.

van Rooijen, A., A. Reniers, J. van Thiel de Vries, C. Blenkinsopp, and R. Mccall, 2012: Modelling swash zone sediment transport at Le Truc Vert beach. *Proc. 33rd Int. Conf. on Coastal Engineering*, Santander, Spain, American Society of Civil Engineers, 1–12, https://doi.org/10.9753/icce.v33.sediment.105.

Watson, G., T. C. D. Barnes, and D. H. Peregrine, 1994: The generation of low-frequency waves by a single wave group incident on a beach. *24th Int. Conf. on Coastal Engineering*, Kobe, Japan, American Society of Civil Engineers, 776–790, https://research-information.bris.ac.uk/en/publications/the-generation-of-low-frequency-waves-by-a-single-wave-group-inci-2.

Zanuttigh, B., and J. W. van der Meer, 2008: Wave reflection from coastal structures in design conditions. *Coastal Eng.*, **55**, 771–779, https://doi.org/10.1016/j.coastaleng.2008.02.009.

Zhang, C., Y. Li, J. Zheng, M. Xie, J. Shi, and G. Wang, 2021: Parametric modelling of nearshore wave reflection. *Coastal Eng.*, **169**, 103978, https://doi.org/10.1016/j.coastaleng.2021.103978.